Building tectonic framework of a blind active fault zone using field and ground-penetrating radar data

Mohamedharoon A. Shaikh [a], Atul K. Patidar [b], Deepak M. Maurya [a,*], Naimisha P. Vanik [a], Akash Padmalal [a], Prabhuti Tiwari [a], Soumyajit Mukherjee [c], Laxman S. Chamyal [a]

[a] *Department of Geology, The Maharaja Sayajirao University of Baroda, Vadodara, 390002, Gujarat, India*
[b] *Department of Petroleum Engineering and Earth Sciences, University of Petroleum and Energy Studies, Dehradun, 248007, Uttarakhand, India*
[c] *Department of Earth Sciences, Indian Institute of Technology Bombay, Powai, Mumbai, 400076, Maharashtra, India*

A R T I C L E   I N F O

A B S T R A C T

Blind active faults may lead to earthquake, therefore their identification and characterization constitute an important structural exercise. Such faults can be mapped by high-resolution shallow subsurface geophysical techniques, which offer meter-scale sub-seismic images. The Kachchh Rift Basin (KRB), situated on the western continental edge of the Indian plate, is tectonically active. The KRB is affected by the reactivation of ~W-striking dip-slip/strike-slip faults. The Kachchh Mainland Fault (KMF) is the largest intra-basinal fault in KRB. The long-term terrain rejuvenation presumably masks the surface expression of the KMF. Shallow subsurface geophysical investigations, assisted by mesoscale structural observations were performed along the western part of the KMF.

A ground-penetrating radar (GPR) was used to decipher the sub-seismic position and geometry of KMF. The KMF is inferred to be a near-vertical north-dipping normal fault. GPR data reveal potential colluvial wedges, faulted alluvial and colluvial Quaternary deposits, small-scale horst-graben and off-fault folding, which are not at all apparent in surficial observations and satellite imageries. A sequential evolution of colluvial wedges is explained attributed to KMF reactivation during Cenozoic. The results suggest that the western part of the KMF is tectonically active, and it should not be overlooked despite low seismicity.

1. Introduction

Blind faults that can activate and cause major earthquakes are critical for seismic hazard assessment (Carpentier et al., 2012a, 2012b; Lunina and Denisenko, 2020). The landscape depositional and erosional processes may remove, cover/conceal, or contrarily, expose active faults (Lunina et al., 2016; Maurya et al., 2021a). Their presence can be inferred through: *(i)* structural studies (Brozzetti et al., 2017: Pollino seismic gap, Italy; Simón et al., 2017: Teruel and Concud faults, eastern Spain; Tokarski et al., 2020: Western Carpathians, Polish Galicia), *(ii)* geomorphological studies (Zygouri et al., 2015: Nisi fault, Greece; Yeager et al., 2019: Matagorda peninsula, United States; Machuca et al., 2021: Yariguíes Range, northern Andes), *(iii)* paleoseismological investigations (Falcucci et al., 2015: Aternro valley fault system, Italy; Li et al., 2018: Milin fault, SE Tibet plateau) and *(iv)* shallow subsurface geophysical investigations (Wang et al., 2003: Mt. Angel fault, USA;

McClymont et al., 2009: Taupo rift, New Zealand; Maurya et al., 2017a: Kachchh Rift Basin, India). The disparity between traditional geological and geophysical techniques occurs where the weak constraints on the subsidiary faults are associated with major faults. Because of soil subsidence, persistent sedimentation and rupture without noticeable slip, blind active faults can be easy to miss (Lunina et al., 2016). In the arid region such as the Kachchh Rift Basin (KRB), the evidence of active faulting and other earthquake-induced structures are easily wiped out in a geological time. Geophysical imaging, therefore, details the geometric expression and slip history of the blind faults (Lunina et al., 2016). Common geophysical methods employed to analyze structures and stratigraphy in the fault zone are: seismic tomography (Sheley et al., 2003; Okada et al., 2019), seismic reflection and refraction (Williams et al., 2003), P-wave velocity tomograms (Carpentier et al., 2012a), gravity (Jiang et al., 2019), vertical electrical soundings, 2D resistivity, electrical resistivity tomography (ERT) (Villani and Sapia, 2017), ground-based magnetic studies (Liberty et al., 2003), magnetotelluric

---

Abbreviations

CMP	Common mid-point	KHF	Katrol Hill Fault
DU	Desalpar Uplift	KHRFZ	Katrol Hill Range Fault Zone
EM waves	Electromagnetic waves	KMF	Kachchh Mainland Fault
FIR filter	Finite Impulse Response filter	KRB	Kachchh Rift Basin
GF	Gedi Fault	NHRFZ	Northern Hill Range Fault Zone
GPR	Ground-penetrating radar	NKF	North Kathiawar Fault
GUF	Gugriana Fault	NPF	Nagar Parkar Fault
IBF	Island Belt Fault	SWF	South Wagad Fault
IBU	Island Belt Uplift	TWTT	Two-way travel time
IIR filter	Infinite Impulse Response filter	VGKNFS	Vigodi-Gugriana-Khirasra-Netra Fault System
		WU	Wagad Uplift

---

investigations (Savvaidis et al., 2012) and ground-penetrating radar (GPR) (Ercoli et al., 2021).

The GPR has been proved to be one of the most promising non-destructive tools to image the blind active faults and associated deformation structures by delivering high-resolution sub-seismic radargrams in a non-invasive and cost-effective manner (e.g., Ercoli et al., 2014; Pousse-Beltran et al., 2018). Trenching is an expensive way to collect data on seismogenic rupture parameters (Lunina et al., 2016; Lunina and Denisenko, 2020). For structural and geomorphological studies, sub-seismic geophysical approaches, particularly the GPR method, combined with outcrop data to calibrate the geophysical signals is a supporting tool for trenching (Lunina et al., 2016; Lunina and Deni-senko, 2020). In the region of continuous sedimentation history, structural outcrops, however, may not expose key deformation structures, which are significant for defining the fault zone and they may have sub-seismic occurrence.

Several GPR-based studies combined with geological field evidence along major faults in the KRB have led to a significantly improved understanding of their nature and neotectonic history (Fig. 1). From north to south, these include *(i)* the Gedi Fault (GF) (Maurya et al., 2013), *(ii)* South Wagad Fault (SWF) (Maurya et al., 2017b), *(iii)* in the Great Rann of Kachchh (Maurya et al., 2006), *(iv)* eastern part of the Kachchh Mainland Fault (KMF) (Chowksey et al., 2011a; Joshi et al., 2012), *(v)* Katrol Hill Fault (KHF) (Patidar et al., 2007, 2008; Maurya et al., 2021b; Tiwari et al., 2021), *(vi)* Vigodi-Gugriana-Khirasra-Netra Fault System (VGKNFS) (Shaikh et al., 2020), *(vii)* the northern coast of the Gulf of Kachchh (Shukla et al., 2008, 2013) and *(viii)* an extensive review work carried out by Maurya et al. (2017a). The results of GPR surveys performed by previous workers are detailed in Supplementary Table S1.

The present study focuses on the detection and imaging the surface as well as sub-seismic geometry of the western part of the W- to NNW-striking KMF employing field structural studies and GPR surveys. The KMF, which is the largest intra-basinal fault, is tectonically active (Maurya et al., 2017a). The KMF is considered to have the greatest seismogenic potential in the KRB, as shown by the destructive 2001 Bhuj earthquake (Shaikh et al., 2019). Secondly, the offshore and onshore areas of Kachchh are critical for hydrocarbon exploration in general (Sen et al., 2019). Understanding the nature of faults onshore and offshore can together provide a complete picture of the hydrocarbon reserve potential of the basin. This makes the KMF so crucial in Kachchh tectonics to understand its nature and geometry by employing various geological and geophysical methods.

The study area is best suited for GPR-based work because of the patchy and isolated rock exposures and scarcity of neotectonic evidence. The prime concern was to evaluate from radargrams whether the impact of any Quaternary movements along the blind KMF could be detected by displacement and/or folding of the near-surface sediments. Shaikh et al. (2019) studied the long-term landscape evolution of the western part of the KMF in response to uplift-induced structurally controlled erosion, due to periodic tectonic movement along the KMF. Former GPR surveys

across the KRB revealed only the major blind active faults (Table S1). In the present work, along with the detection of the major blind fault, associated deformation structures are detected in the fault zone. With the aid of radargrams, a multitude of secondary active faults in the KMF zone have been identified. The study has implications for understanding neotectonics and seismic hazard estimation related to the KMF.

2. Tectonics of the Kachchh Rift Basin (KRB)

The state of Gujarat, at the western continental margin of India, can be geographically divided into *(i)* the mainland Gujarat in the east, *(ii)* KRB to the NW (Maurya et al., 2017a; Shaikh et al., 2020) and, *(iii)* Saurashtra peninsula to the SW (Vanik et al., 2018, 2020). The W-striking pericratonic KRB is currently undergoing active co-seismic deformation (Maurya et al., 2017a; Shaikh et al., 2020) (Fig. 1). The structural framework of the KRB is dominated by parallel ~ W-striking intra-basinal faults. From north to south, these are: Island Belt Fault (IBF), GF, SWF, KMF (>1200 m throw) and KHF (~732 m maximum throw) (Biswas, 1993) (Fig. 1). These major, near-vertical faults display narrow flexures and have accommodated large-scale uplifts: Island Belt Uplift (IBU), Desalpar Uplift (DU), ~60 km long and ~40 km wide Wagad Uplift (WU), ~193 km long and ~72 km wide Kachchh Mainland Uplift (KMU) (Biswas, 1993) (Fig. 1). The KMU is sub-divided into four structural zones: the Northern Hill Range Fault Zone (NHRFZ) along the KMF, Katrol Hill Range Fault Zone (KHRFZ) along the KHF, VGKNFS and Bhuj structural low (Biswas, 1993; Shaikh et al., 2020; Maurya et al., 2021b) (Fig. 1). W-striking, intra-basinal faults are affected and segmented by NW- to NE-striking, m to km-scale, transverse faults with dip-/oblique-slip deciphered in the field (Maurya et al., 2003a; Shaikh et al., 2020).

During the Late Triassic or Early Jurassic, before India-Africa separation, the KRB rifted, which generated extensional stresses and experienced constant sedimentation until the Late Cretaceous (Biswas, 2016; Shaikh et al., 2020). As a result, the W-striking major faults and other subsidiary faults were activated as normal faults (Biswas, 2016). The rifting of the KRB was then aborted during Late Cretaceous (Biswas, 2016). The drift of the Indian plate started with counter-clockwise rotation from Mid-Jurassic onward after the break-up of the Gondwanaland and India-Africa separation (Biswas, 2016). This caused trans-tension in the KRB (Biswas, 2016). Since the Late Cretaceous, rifting of the KRB was followed by rift inversion, leading to reactivation of intra-basinal faults as reverse faults (Shaikh et al., 2020). During the post-Cretaceous inversion, particularly within the Neogene and Quaternary times, the faults reactivated periodically that promoted the accumulation of Cenozoic sediments (Biswas, 1993, 2016).

In the seismic hazard zonation index, KRB, one of the most earthquake-prone intra-plate regions in India, falls into the highest seismic risk zone–V (BIS, 2002; Choudhury et al., 2018). All the major faults are considered tectonically active, characterizing the KRB as the one with potentially multiple seismic origins. The KRB has witnessed
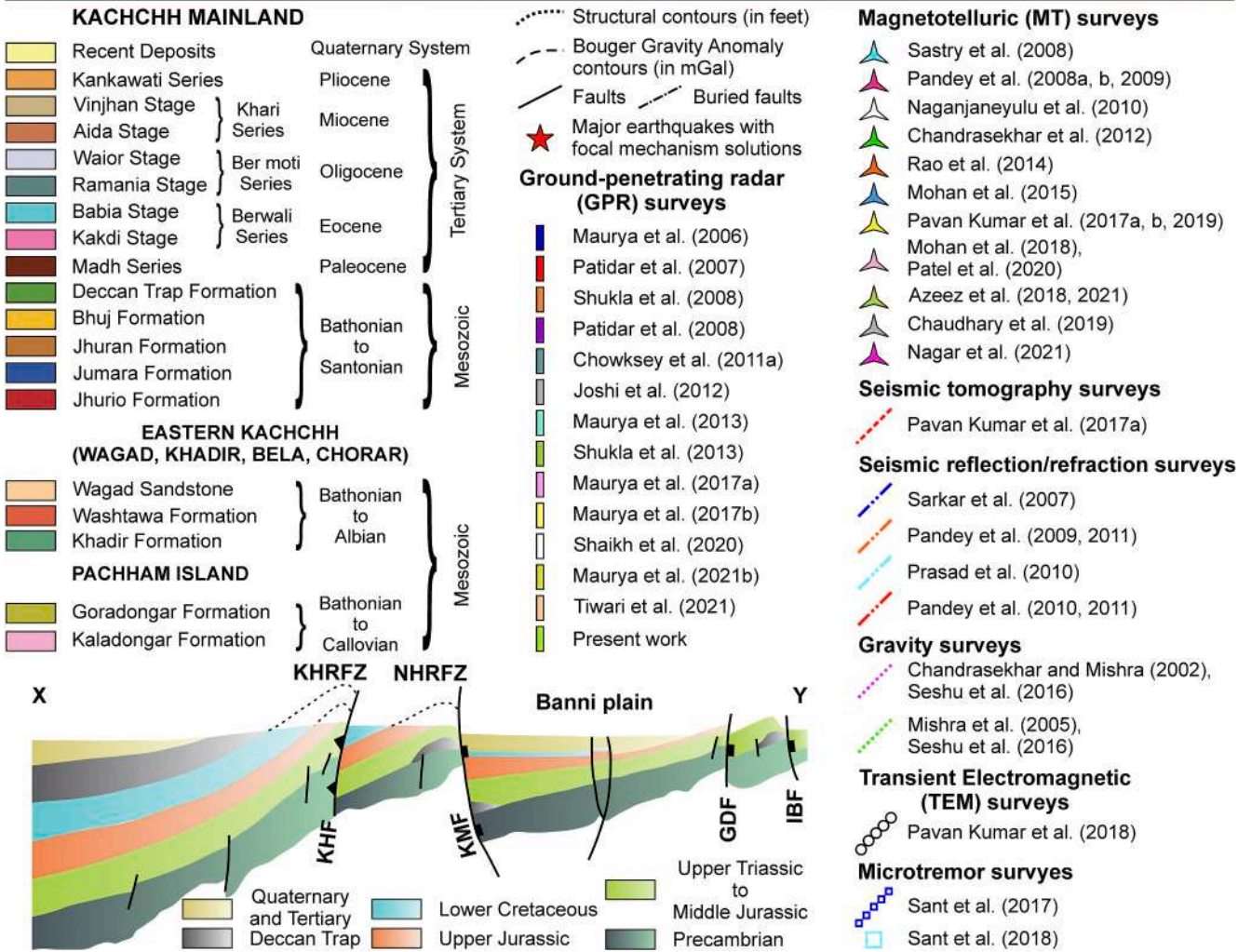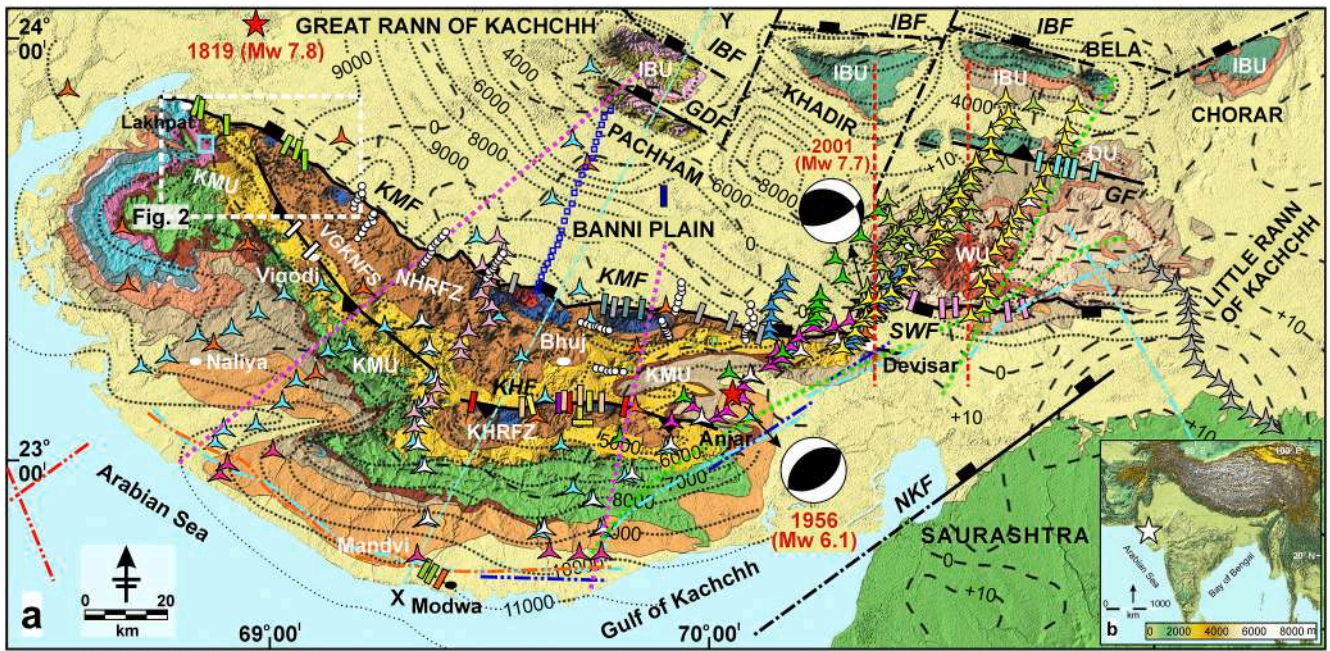
(caption on next page)

Fig. 1. (a) Geological map of the Kachchh Rift Basin (KRB) (reproduced from Shaikh et al., 2020). Geological and structural details are based on (Biswas, 1993). The study area is denoted by a white dashed rectangle. The black dotted lines represent structural contours drawn over the top of Precambrian basement with a 1000 feet (values are in negative) contour interval (Biswas, 1993). The black dashed lines reflect Bouger Gravity Anomaly contours in mGal (Dasgupta et al., 2000). The locations of major earthquakes in the KRB with focal mechanism solutions are shown by red stars (Chung and Gao, 1995; Rastogi et al., 2001). The locations of geophysical surveys are marked by various symbols in the map. Ground-penetrating radar (GPR) surveys- Maurya et al. (2006), (2013), (2017a, b), (2021b); Patidar et al. (2007), (2008); Shukla et al. (2008), (2013); Chowksey et al. (2011a); Joshi et al. (2012); Shaikh et al. (2020); Tiwari et al. (2021). Magnetotelluric (MT) surveys- Sastry et al. (2008); Pandey et al. (2008a, b), (2009); Naganjaneyulu et al. (2010); Chandrasekhar et al. (2012); Rao et al. (2014); Mohan et al. (2015), (2018); Pavan Kumar et al. (2017a, b), (2019); Patel et al. (2020); Azeez et al. (2018), (2021); Chaudhary et al. (2019); Nagar et al. (2021). Seismic tomography surveys- Pavan Kumar et al. (2017a). Seismic surveys- Sarkar et al. (2007); Pandey et al. (2009), (2010), (2011); Prasad et al. (2010). Gravity surveys- Chandrasekhar and Mishra (2002); Mishra et al. (2005); Seshu et al. (2016). Transient Electromagnetic (TEM) investigations- Pavan Kumar et al. (2018). Microtremor surveys- Sant et al. (2017), (2018). Follow Table S1 (Supplementary data) for further information. IBF: Island Belt Fault, GDF: Gora Dungar Fault, GF: Gedi Fault, SWF: South Wagad Fault, KMF: Kachchh Mainland Fault, VGKNFS: Vigodi-Gugriana-Khirasra-Netra Fault System, KHF: Katrol Hill Fault, NKF: North Kathiawar Fault, IBU: Island Belt Uplift, DU: Desalpar Uplift, WU: Wagad Uplift, KMU: Kachchh Mainland Uplift, NHRFZ: Northern Hill Range Fault Zone, KHRFZ: Katrol Hill Range Fault Zone. Slip-sense of uplift-bounding and intra-uplift faults is based on Biswas (1993); Maurya et al. (2017a); Shaikh et al. (2020); Tiwari et al. (2021). The schematic cross-section X–Y is redrawn from Biswas (1993). (b) Map of Indian plate with a white star indicating the location of the KRB. (For interpretation of the references to color in this figure legend, the reader is referred to the Web version of this article.)

several devastating moderate–high magnitude intra-plate earthquakes attributed to periodic tectonic movement along the major faults. A few examples are the 1819 Allah Bund earthquake (Mw 7.8; 15 km focal depth; Bilham, 1999; Rajendran et al., 2001; Padmalal et al., 2019), 1956 Anjar earthquake (Mw 6.1; 15 km focal depth; Chandra, 1977; Chung and Gao, 1995) and 2001 Bhuj earthquake (Mw 7.7; 23 km focal depth; Bendick et al., 2001) (Fig. 1). Several geophysical studies have been carried out to decipher the subsurface information in the KRB (Fig. 1). Follow Table S1 (Supplementary data) for further information.

3. Kachchh Mainland Fault (KMF) and Northern Hill Range Fault Zone (NHRFZ)

In the tectonically active regions like KRB, the KMF scarp, which leaves the fault block on the southern side topographically higher than its northern counterpart is a common landform manifestation of active faults. The NHRFZ is a fault-parallel flexure zone that demarcates the upthrown block of the KMF (Biswas, 1993) (Figs. 2 and 3). Continuous slip along the NNW- to W-striking KMF in different tectonic phases in geological time scale and syn-rift magmatism since the Late Cretaceous in the KRB produced a linear chain of discontinuous, asymmetric domal, anticlinal structures and drape folds in the NHRFZ (Biswas, 1993; see the model in Shaikh et al., 2019). The southern limbs of the domes show gentle dips and northern limbs show near-vertical dips owing to the tectonic deformation along the KMF.

The seismically active near-vertical KMF originated during the Mesozoic (Biswas, 1993). The KMF is traceable for >150 km in the field and in remote sensing images as a north-facing steep discontinuous scarp, delineating the rugged rocky topography of the NHRFZ in the upthrown block (Biswas, 1993; Shaikh et al., 2019; Padmalal et al., 2021). The northern downthrown block comprises the Holocene sedimentary basin of the Great Rann. In the westernmost part, from Lakhpat to Manjal, the KMF swings from NNW–W as it is laterally displaced by several NW- to NE-striking transverse faults with dip-/oblique-slip mostly located in the inter-domal saddle zones. The study area covers the KMF zone to the northeast of several domes (Figs. 2 and 3). The surface trace of the KMF is marked by near-vertical Mesozoic rocks mostly sandstones/shale, forming the northern limbs of the domes and steep north-dipping Tertiary rocks (limestone, shale, clays, conglomerate) jutting out of the Rann and alluvial sediments. Therefore, the KMF is identified as the lithotectonic contact between the Mesozoic and Tertiary rocks. This is confirmed by the patchy exposures of the KMF, which provide ground truth for the interpretation/correlation of GPR data.

We constructed WNW- to NE-oriented swath profiles derived from Google Earth imageries to extract information about uplift pattern in the topography of the western part of the NHRFZ (Fig. 3). The best approach to assess the fault-throw distribution is to conduct topographic analysis around active fault scarps (Shaikh et al., 2019). The detection of scarp is

not always clear, due to the irregular denudation rate and, soft and poorly consolidated sediments in the Rann surface towards the downthrown block. The KMF scarp is a steep north-facing scarp that separates the rugged rocky topography of the structural domes (P1 in Fig. 3). Note that how the topography gradually diminishes on either side of the P1 swath. The inter-domal regions in P1 swath are marked by the north-flowing rivers. The scarp abruptly rises against the flat Quaternary surface of the Great Rann (P2–P8 in Fig. 3). The scarp thus acts as the sharp physiographic divide between the flat surface of the Great Rann in the northern downthrown block and rugged hilly topography in the southern upthrown block. The KMF scarp is irregular and developed over steep north-dipping Mesozoic rocks that create the northern limbs of domes. P2–P8 swaths clearly show the low-lying KMF scarp, rugged hilly topography over the domes and relatively higher relief of the Jaramara scarp and Ukra intrusive. The present-day KMF scarp is thus a retreated fault scarp, with the actual trace lying further north and buried under Quaternary sediments of the Great Rann. Therefore, the actual location of the KMF in the subsurface farther north from the structural domes is evaluated by extensive GPR surveys.

The E-striking, ~1.6 km long, linear, elongated Lakhpat dome is located on the westernmost extremity of NHRFZ (Biswas, 1993). The KMF truncates the northern end of the Lakhpat dome (Fig. 4a and b). The Lakhpat dome exposes steep to gentle north-dipping Mesozoic Ferruginous sandstone. Narrow strips of steep north-dipping Tertiary limestone can be observed in the fault zone. The litho-contact in between these two lithologies mark the ~W-striking KMF with normal slip. The ferruginous fault gouge also draws attention to the location of KMF (Fig. 4a). SE of Lakhpat dome, finely powdered and partially bleached fault gouge marks the KMF where Mesozoic sandstone are exposed on SW side and Tertiary limestones are exposed on NE side (Fig. 4c, f).

The oval-shaped Karanpur dome is located towards SE of Lakhpat dome (Biswas, 1993) (P1, P2 in Fig. 3). The NNW-striking and NE-dipping KMF with normal slip is located on the NE side of Karanpur dome (Fig. 4d). NNW-striking and near-vertical Eocene limestone is in contact with ferruginous sandstone, which characterize the flexure zone. The exposure is capped by ~2 m thick titled fluvially-reworked miliolite deposits (Fig. 4e). This is the only exposure in the study area where Quaternary deposits capping the KMF could be located. No slickenside kinematic indicators and lineations were observed. We believe that ~2–4° titling of miliolite deposits to NE side is attributed to the neotectonically active nature of KMF and may represent instantaneous/co-seismic response of off-fault tectonic deformation (see Table 1.2 of McCalpin, 2009) (Fig. 4d and e). Further SE, the KMF zone is marked by near-vertical Mesozoic sandstones that looks like a zone of a fault gouge exposed to the west, while Tertiary limestones are exposed to the east (Fig. 4g). N115°-striking thin stripes of near-vertical Eocene limestone jutting from the flat soil surface between the Lakhpat and Ghuneri dome abruptly end up against steep Mesozoic Ferruginous sandstone, which distinctly marks the KMF (Fig. 4h).
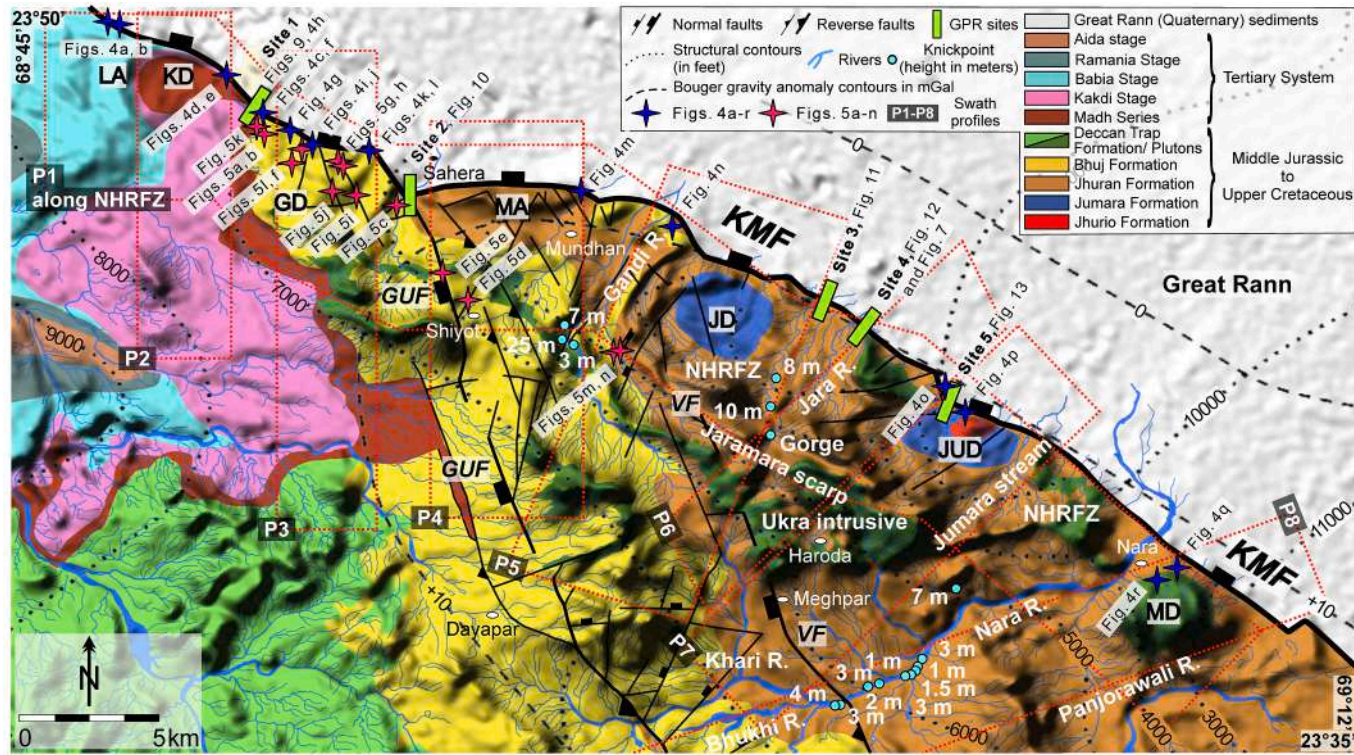
Fig. 2. Morphostructural map of the present study area. Sites 1–5: GPR survey sites denoted by green bars. The size of the bars is highly exaggerated. P1–P8: locations of the eight swath profiles indicated by rectangles with red dotted lines. Blue and red stars: location of Fig. 4a–r and 5a–n respectively. The knickpoints are marked by blue circles with their heights indicated. Black dotted lines: structural contours drawn over the top of Precambrian basement with a 1000 feet (values are in negative) contour interval (Biswas, 1993). Black dashed lines: Bouger Gravity Anomaly contours in mGal (Dasgupta et al., 2000). KMF: Kachchh Mainland Fault, GUF: Gugriana Fault, VF: Vigodi Fault, NHRFZ: Northern Hill Range Fault Zone, LA: Lakhpat Anticline, GD: Ghuneri Dome, MA: Mundhan anticline, JD: Jara Dome, JUD: Jumara Dome, MD: Manjal Dome. (For interpretation of the references to color in this figure legend, the reader is referred to the Web version of this article.)
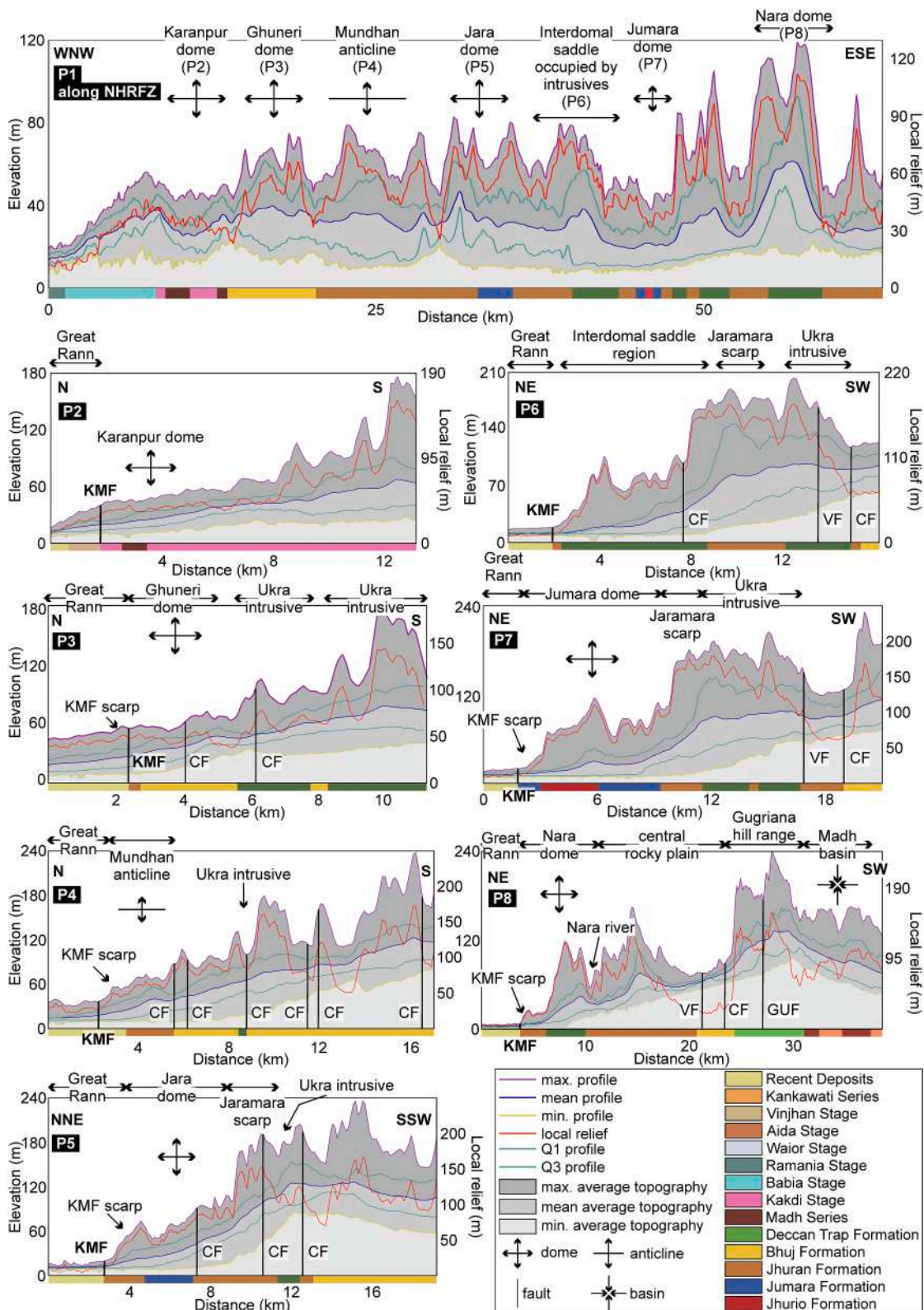
Fig. 3. Swath profiles (P1–P8) extracted from SRTM v.3 data. P1: along ~ WNW-striking NHRFZ, P2–P8: across Karanpur dome, Ghuneri dome, Mundhan anticline, Jara dome, inter-domal saddle region occupied by Ukra intrusives, Jumara dome and Nara dome. Locations of the swaths are depicted in Fig. 2. NHRFZ: Northern Hill Range Fault Zone, KMF: Kachchh Mainland Fault, CF: Cross Fault, VF: Vigodi Fault, GUF: Gugriana Fault. Since P1–P8 are not the cross-sections, the faults are marked by vertical lines, which ignore their attitude. Underneath each swath is a color bar representing lithology. The regions of dark grey, grey and light grey in each swath reflect the maximum, mean and minimum average topography. (For interpretation of the references to color in this figure legend, the reader is referred to the Web version of this article.)

(caption on next page)

Fig. 4. (a) W-looking view of near-vertical Mesozoic sandstone exposed on the ~W-striking Lakhpat anticline. (b) NNW-looking view of the north-flowing stream between Lakhpat anticline and Karanpur dome. The cliff exposes gently north-dipping Mesozoic ferruginous sandstone. Note the presence of Tertiary limestone in the background. (c and f) NE-looking view of the KMF with normal slip-sense (attitude: N340° strike, N70° dip direction and 80° dip) acting as a lithotectonic contact between Mesozoic sandstone and Tertiary limestone. (d) At the eastern fringe of the Karanpur dome, the Mesozoic-Tertiary lithotectonic contact (attitude: N140° strike, N50° dip direction and 85° dip) highlights the KMF. (e) Close-view of titled fluvial miliolites capping the lithotectonic contact. (g) NE-looking view of the KMF Zone marked by near-vertical beds indicate potential fault gouge. (h) W-looking view of the GPR survey site 1, east of the Karanpur dome. ~SW-oriented transect marked by white dashed line crossing ~ NNW-striking KMF marked by black dashed line. (i) Eocene nummulitic limestone (attitude: N285-310° strike, N15-40° dip direction and 85–88° dip) exposed at the NW flank of Ghuneri dome. (j) Tertiary limestone (attitude: N85° and N88° strike, N175° and N178° dip direction, 88° and 85° dip) exposed north of NE limb of Ghuneri dome. Ridge exposing ferruginous Mesozoic sandstone can be observed at the far side of the photograph. (k) Overturned flexure observed on the northern flank of the Ghuneri dome as the NW-striking ferruginous sandstone (attitude: N120° and N123° strike, N210° and N213° dip direction, 78° and 65° dip) are inverted and dip steeply towards south. (l) Near-vertical Mesozoic sandstone (attitude: N297° strike, N27° dip direction and 87° dip) exposed in the KMF zone at the eastern flank of Ghuneri dome. (m) South-dipping fault with indeterminate slip-sense exposed east of Mundhan anticline (attitude: N70° strike, N160° dip direction and 45° dip). (n) East-dipping Mesozoic sandstone (attitude: N330-30° strike, N60-120° dip direction and 24–34° dip), exposed east of Mundhan anticline. The KMF is further north of this location. (o) Jhuran sandstone (attitude: N276° and N275° strike, N6° and N5° dip direction, 86° and 88° dip) jutting from the Great Rann surface. (p) NE-striking faulted dyke (attitude: N55° strike, N145° dip direction and 43° dip) exposed to the north of Jumara scarp. (q) Northern limb of the Manjal dome exposing ~50 m high and ~3.5 km long KMF scarp. The KMF is further north of the scarp buried below Rann surface. (r) Northern limb of the Manjal dome intruded by ~ NW-dipping igneous rocks. The inferred KMF is highlighted by black dashed lines in Figs. a–d, g and h. See geological map of the study area in Fig. 2 for the location of Fig. 4a–r.

The ferruginous sandstone and ironstone bands and patchy occurrence of shale belonging to the Bhuj Formation crop out rhythmically with swerving strike in the Ghuneri dome (location in Fig. 2). The near-vertical KMF cuts the steep northern flank of Ghuneri dome (P3 in Fig. 3). To the north of the western flank of Ghuneri dome, the KMF zone characteristically strikes E to ENE, with near-vertical beds of Eocene nummulitic limestone resting against the steep Mesozoic ferruginous sandstone (Fig. 4i). On the eastern flank of Ghuneri dome, the E-striking inverted Tertiary massive limestones (dip 85–88° towards south) (Fig. 4j) are in lithotectonic contact with NW-striking near-vertical Mesozoic ferruginous sandstone in the south (Fig. 4l). Overturned flexure has also been observed on the northern flank of Ghuneri dome as the NE-striking ferruginous sandstone beds are inverted and dip steeply towards SW (Fig. 4k). WNW-striking KMF with indeterminate slip-sense is exposed near eastern flank of Mundhan anticline (Fig. 4m). (i) East-dipping Mesozoic sandstone, exposed east of Mundhan anticline (Fig. 4n), (ii) northern limb of the Manjal dome exposing Mesozoic sandstone (Fig. 4q) and, (iii) northern limb of the Manjal dome intruded by ~ NW-dipping igneous rocks (Fig. 4r) indicate that the KMF is further north of the scarp buried below Rann surface. The approximate position of the KMF can be marked by (i) near-vertical Jhuran sandstone jutting from the Great Rann surface (Fig. 4o) and, (ii) faulted dyke exposed to the north of Jumara scarp (Fig. 4p).

4. Significance of cross-faults

Each of the folded structural elements of the NHRFZ is affected by variably striking transverse faults with dip-/oblique-slip. This fault network is inherited from the extensional stress regime of the KRB. The intra-domal and inter-domal faults are observed that either obliquely meet, or displace the KMF, or otherwise terminate against the KMF. As the transverse faults are well-exposed, there was no need to perform a GPR survey across these faults. None of the intra-domal or inter-domal faults (Fig. 5) is capped by the Quaternary sediment cover.

The NW-/NE-striking inter-domal faults occupy the structurally low-lying saddle region, which separates the domes with differential uplift in the NHRFZ. About 600 m WNW of Ghuneri dome, the W-striking non-striated extensional fault was encountered in the Bhuj sandstone (Fig. 5a and b). The hangingwall block marks locally the occurrence of normal drag folding, which possibly indicates normal slip-sense. Another NE-striking transverse fault with indeterminate slip-sense was encountered in the saddle region between the eastern flank of Ghuneri dome and western flank of Mundhan anticline (Fig. 5c). Its NE end terminates along the NW–W striking KMF. About 3.5 km south of the E-striking Mundhan anticline, NE-striking non-striated extensional fault is encountered (Fig. 5d). The southern side of the fault ends up in the NNW-striking GUF. Whereas the northern end of this ~2.3 km long fault

ends with another transverse fault striking NW. At the road-cut section, the fault disturbs the almost horizontal stratigraphic units at the high oblique angle with an estimated throw of ~85 cm (Fig. 5d). The stratigraphic units are composed of bleached and ferruginous varieties of sandstones and shales belonging to the Bhuj Formation. The main structural components such as the fault core and principal slip surface (Y-plane) are observed. The principal slip surface is well-exposed in the lowermost ferruginous sandstone unit overlain by bleached to purplish shale. The fault core marks the limits of the concentrated shear zone and consists of the highly deformed host rock material of mainly sandstone and shale. It turns abruptly into undeformed host rock outside the width of the fault core, indicating a narrow width of the damage zone. The northernmost occurrence of the NW-striking GUF crops out in the Bhuj sandstone, ~2 km south of the western flank of the Mundhan anticline (Fig. 5e). The GUF shows oblique-slip with normal dip-slip and dextral strike-slip components (Shaikh et al., 2020).

W- to NE-striking intra-domal faults with normal/oblique-slip kinematics, which die out in the vicinity of the W-striking KMF, are prevalent in the Ghuneri dome, Mundhan anticline and Jara dome (Fig. 5g–i, k–n). The stress regime or tectonic events responsible for the movement along the non-striated intra-domal faults in Fig. 5g–i, k and l is difficult to decipher as they occur in uniform lithology. The intra-domal faults dip steeply (60–85°) and often run oblique to the strike of Jhuran/Bhuj sandstone/shale. This criteria assisted in identifying the intra-domal faults and distinguishing them from joints. In satellite imageries, the intra-domal faults are observed to displace in the strike-slip domain the rhythmic bands of ferruginous sandstone and shale in Ghuneri dome, Mundhan anticline and Jara dome. The trend of one of the joint sets correlates well with the N270°-striking transverse fault exposed nearby at the NW fringe of the Ghuneri dome (Fig. 5j).

The elliptical Mundhan anticline, located E of the Ghuneri dome, has been affected by numerous WSW- to NE-striking oblique-slip transverse faults and displace the W-striking parallel to sub-parallel linear ridges, as seen in the satellite view. Of them, the NW-striking faults are more prominent. The longest of them extends for ~9 km, which meets the KMF near the western flank of the Mundhan anticline. They extend southward beyond the confines of the Mundhan anticline and merge in the VGKNFS (Fig. 2). In ground view, it appears as if the NE-striking faults are truncated by the NW-striking faults forming a distinct Y-pattern (Biswas, 1993). The NW-striking oblique-slip fault running in the inter-domal saddle region between the Ghuneri dome and Mundhan anticline has been responsible for the sudden change in the strike of the KMF from ~NW in the Sahera to west in the vicinity of the Mundhan anticline. NE-striking intra-domal extensional faults are exposed in Bhuj sandstone at the SW fringe of the Jara dome (Figs. 5m, n). Fig. 5e of Shaikh et al. (2019) incorrectly concluded reverse slip-sense of the fault shown here in Fig. 5n. The drag fold formed in the hangingwall is convex
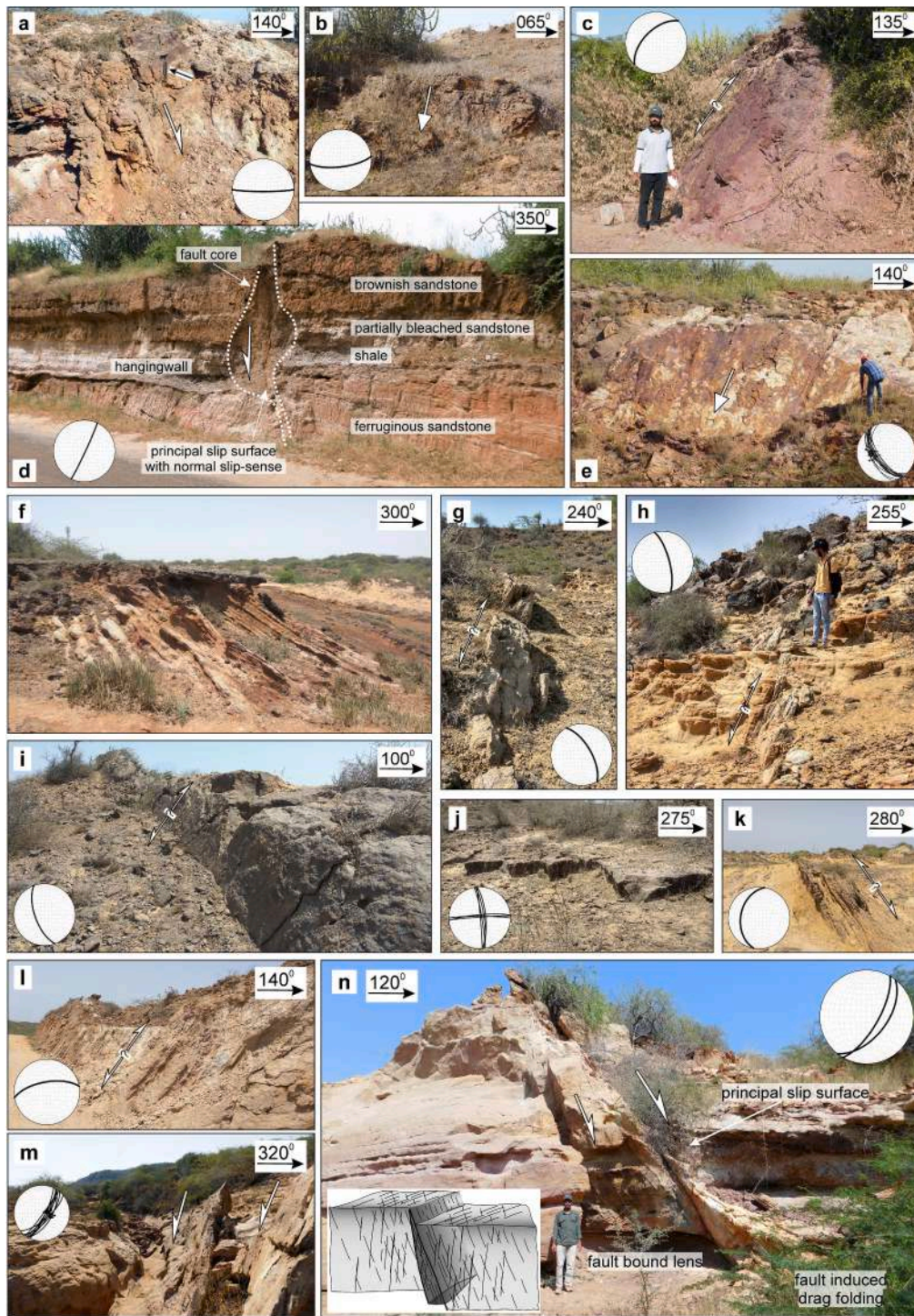
Fig. 5. (a) and (b) Non-striated normal fault exposed ~600 m WNW of Ghuneri dome (attitude: N90° and N83° strike, N180° and N173° dip direction, 85° and 72° dip). The hammer is pointed out by a black full arrow. (c) Non-striated fault with indeterminate kinematics (attitude: N37° strike, N315° dip direction and 57° dip) exposed east of Mundhan anticline. (d) ~350 cm high outcrop exposure of the NE-striking extensional fault (attitude: N205° strike, N115° dip direction and 87° dip) exposed ~3.5 km south of Mundhan anticline. White dotted lines outline key structures. (e) NW-striking GUF with oblique slip exposed ~2 km south of western flank of Mundhan anticline. (f) Angular unconformity located at the western limb of the Ghuneri dome. (g-i, k and l) Small-scale intra-domal transverse faults with indeterminate slip-sense exposed within Bhuj sandstone of the Ghuneri dome. (g) Fault attitude: N350° strike, N60° dip direction and N65° dip. (h) Fault attitude: N345° strike, N72° dip and N75° dip direction. (i) Fault attitude: N340° strike, N65° dip and N250° dip direction. (j) Two sets of near-vertical joint planes in Bhuj sandstone at the southern extremity of the Ghuneri dome (average trend: N350° and N270°). (k) NNE-striking transverse fault at the NW limb of the Ghuneri dome (attitude: N190° strike, 40° dip and 280° dip direction). (l) ~W-striking transverse fault at the western extremity of the Ghuneri dome (attitude: N80° strike, 65° dip and N350° dip direction). (m) and (n) NE-striking transverse faults with normal slip exposed at the SW fringe of the Jara dome. (m) The normal fault with a vertical throw of ~7 m affects a 7 m deep gorge on one side. (n) The principal slip surface and subsidiary slip plane (attitude: N30° and N38° strike, N120° and N128° dip direction, 70° and 55° dip) bound a lensoidal structure. The principal slip surface has formed a darg fold in the hangingwall. The outcrop is affected by a dense network of deformation bands as seen in the inset sketch. See geological map of the study area in Fig. 2 for the location of Fig. 5a–n.
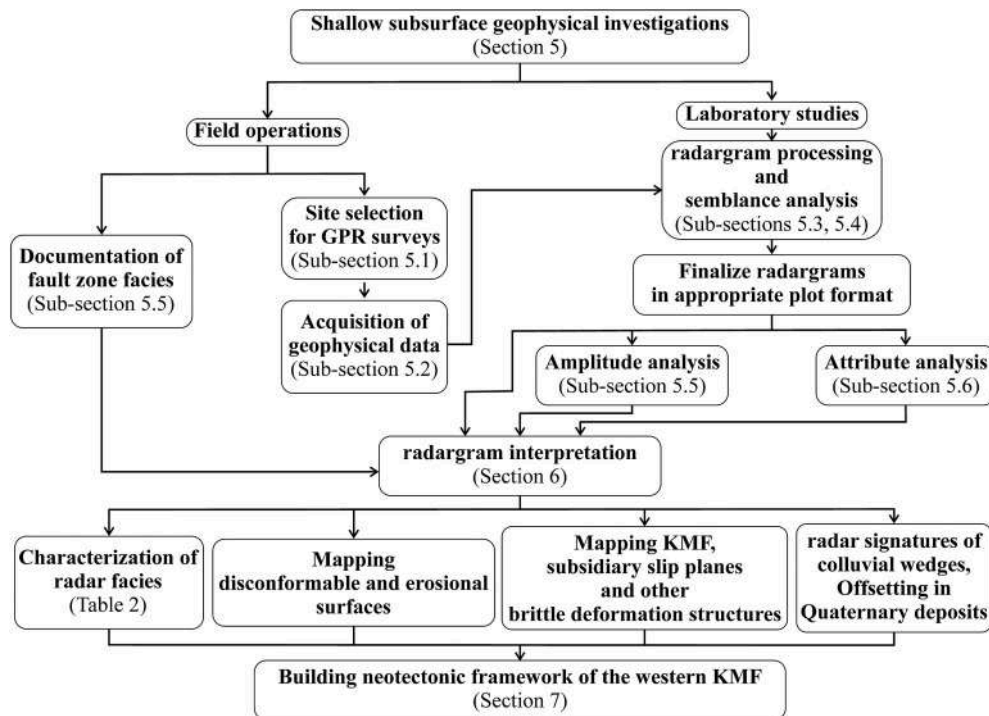
Fig. 6. Flow chart showing the methodology followed in the present study.

towards the slip direction, implying that normal drag occurred along a normal fault. The subsidiary slip plane bifurcating from the principal slip surface bound a fault lens tapering upwards.

5. Ground-penetrating radar (GPR) survey methodology

The GPR creates high-resolution radargrams of the shallow (generally a few meters) subsurface in a non-destructive manner that superficially mimic seismic reflection images (Jol, 2009). The GPR and seismic surveys commonly use the transmitted waves that are reflected and then recorded at the surface by a receiver (Jol, 2009). Unlike compressional elastic waves used in the seismic surveys, electromagnetic (EM) waves are used to carry out a GPR survey (Jol, 2009). 2D GPR is a cost-effective and rapid geophysical technique to investigate and image the geological discontinuities such as faults, deformation bands, fractures and associated deformed sedimentary structures (McClymont et al., 2010; Lunina and Denisenko, 2020; Shaikh et al., 2020). GPR uses the propagation, reflection and scattering of 10–1000 MHz frequency EM waves in geological applications (Jol, 2009). The method depends on the contrast of dielectric properties of the rock interfaces in the subsurface (Jol, 2009). The depth of investigation depends on the degree of attenuation of EM waves and the antennae frequency being used. The lower the frequency, the greater is the penetration depth, which varies from a few centimeters in conductive materials and can go up to tens of meters in low conductivity media (Davis and Annan, 1989; Jol, 2009). See the flow chart in Fig. 6 for the detailed methodology followed for GPR investigations.

5.1. Aim and planning of GPR survey

As per the published literature and detailed field investigations carried out in the present study (Follow Section 3), the blind KMF acts as a lithotectonic contact between the Mesozoic sandstone/shale and Tertiary limestone (Maurya et al., 2003b). The W- to NE-striking intra-domal and inter-domal oblique-slip faults are well-exposed in the study area, away from the KMF and do not need to be mapped by a GPR survey (Fig. 5, Section 4). Therefore, radargrams were recorded along five

pre-defined transects perpendicular to the KMF strike to: *(i)* detect the position and geometry of the blind KMF up to 10 m depth, *(ii)* map the continuity of the KMF and, *(iii)* understand the distribution of secondary faulting within the deformation zone. The planned survey sites are located between Lakhpat in the west and Manjal dome in the east (Fig. 2).

5.2. Acquisition of geophysical data

The radargrams presented in this work were acquired by 200 MHz frequency shielded mono-offset antenna connected with single-channel Subsurface Interface Radar-20 (SIR-20) system manufactured by GSSI Inc. USA (Fig. 6). It provided satisfactory results in terms of penetration depth and data resolution required to study the near-surface fault properties. The Common Mid-Point (CMP) gathers were acquired by using unshielded multi-offset 80 MHz frequency antenna to estimate the propagation velocity of EM waves. Radargrams were acquired in continuous mode by connecting the 200 MHz antenna to the survey wheel to measure the distance between traces. Whereas, CMP gathers were collected in point mode with 10 cm step size and 1 m initial distance. During the survey planning, it was decided to keep the surveying transect perpendicular to the fault strike to get a vivid image of the subsurface deformation structures. Several radargrams were collected along the same transect to determine the most suitable header parameters for the particular terrain. During the survey, a marker was assigned manually to the radargram at an inferred topographic location of the fault. This aided us to determine the approximate position of the fault in the radargram during data analysis. The fault position was further confirmed by observing the changes in the reflection patterns (Section 6).

5.3. Processing of GPR data

Radargrams recorded were severely affected by high amplitude noise. In some cases, sharp vertical bands of low-frequency were prevalent. Raw radargrams often show long, continuous flat reflections of system ringing noise (Supplementary Fig. S1). This could be owing to the

Table 1

Summarized data sheet of GPR survey acquisition and processing parameters for five sites.

Survey parameters		Survey sites				
		Site 1 (Fig. 9)	Site 2 (Fig. 10)	Site 3 (Fig. 11)	Site 4 (Fig. 12)	Site 5 (Fig. 13)
GPR data acquisition parameters						
Direction		N40°	N355°	N30°	N45°	N30°
Nominal antenna frequency (MHz)		200	200	200	200	200
Profile length (m)		22	~40 (49.5 m initial lengh)	32 (42 m initial lengh)	30 (45 m initial length)	24 (40.3 initial length)
Number of scans		1525	3450	3360	3600	3225
Scans/sec		64	64	64	64	64
Time window (ns)		100	100	150	150	150
Depth (m)		6	6	7.5	8	8
Number of samples		512	512	512	512	512
Dielectric constant		6.00	6.00	6.00	6.00	6.00
Radargram processing parameters						
Time-zero correction (ns)		7.85	8.24	13.54	13.83	13.24
Background removal (scans)		1023	1023	1023 (between 40 and 512 samples)	1023	1023
Band-pass frequency filtering	IIR horizontal (scans)	5, 3, 2	5, 3, 2	5, 3, 2	5, 3, 2	5, 3, 2, 7
	FIR vertical High pass (MHz)	–	–	100, 50	60	50
	Low pass (MHz)	–	–	440	310, 240	440, 310, 240
Range gain (linear function)		2	2	3	2	2

instability of the equipment while dragging and vibrations caused by antenna-ground coupling during survey operations (Green et al., 2003; Shan et al., 2015). Therefore, processing of raw radargrams was required as the data were affected by different kinds of noise (Fig. 6).

The post-survey processing was performed in RADAN (v.7) software by GSSI Inc. The processing steps below were followed to obtain the best visual representation of radargrams to appreciate and interpret the geological features: time-zero correction, background removal, band-pass frequency filtering, range gain, semblance analysis and time-to-depth conversion (Jol and Bristow, 2003; Cassidy, 2009; Jol, 2009). All the radargrams were collected on a flat topography, thus there was no need to correct for elevation differences. Based on average subsurface radar wave velocity of 0.12 m ns^{-1} (Follow Sub-section 5.4), radar arrivals have been translated to time-depth. Note that the direct air and ground waves have been muted in each of the radargram formats. Each of the processing steps is detailed in Supplementary data. Table 1 summarizes the GPR data acquisition and processing parameters utilized.

5.4. Semblance analysis

The subsurface EM waves velocity is important for conversion of two-way travel time (TWTT) to accurate estimation of depth. The standard approach to estimate the EM wave velocity is to carry out the CMP survey. We acquired several CMP gathers using 80 MHz bi-static antennae configuration to estimate the propagation velocity of EM waves in the subsurface. The individual reflection events were picked manually and the estimated average velocity of 0.12 m ns^{-1} was derived, corresponding to a dielectric constant of 6 (Fig. 7). This value has been used for time to depth conversion of all the collected radargrams.

5.5. GPR amplitude analysis and radar facies characterization

The sedimentary facies associations of the Mesozoic Jhuran and Bhuj Formation, Tertiary rocks and overlying Quaternary deposits have been widely discussed (Biswas, 1993, 2016). Chowksey et al. (2011a, b) extensively described the Quaternary stratigraphy exposed in the eastern KMF. They are found to be useful to understand the exposed stratigraphic sequences in the western KMF and to correlate them with the radar facies. Guha et al. (2020) followed a reflectance

spectroscopy-guided approach to map the glauconitic clay-bearing zones within Tertiary limestones in the western part of the KRB. Note that the GPR response to clay-rich lithology is poor (Ékes and Friele, 2003; Magalhães et al., 2017).

Fig. 8 presents the variety of lithologies exposed in the NHRFZ. Note that the GPR survey sites are farther north from the cliff exposures shown in Fig. 8. Such lithology is presumably still exposed at the GPR survey sites, but it is now buried under Holocene Rann sediments cover. The Jara river originates from the backslope of the Jaramara scarp and meets the Great Rann in the north (Fig. 2) (Shaikh et al., 2019). The river is incised by ~30 m into the Mesozoic Jhuran sandstone-shale intercalation overlain by fluvially reworked miliolites, deposited over an erosional surface (Fig. 8a). Notice the exposure of an aeolian miliolite in the foreground and appearance of the Jaramara scarp in the background. The stream west of the Jara river flows in the low hilly topography of the Jara dome (Shaikh et al., 2019). The incised cliff exposes ~2 m thick clast-supported colluvio-fluvial Quaternary miliolite deposits covering the top surface (Fig. 8b). It is underlain by ~5.5 m thick thinly-bedded Jhuran sandstone-shale intercalated deposits. Tertiary limestones are exposed in the form of a mound near the Karanpur dome (Fig. 8c).

The cliff sections of rivers that pass through the eastern NHRFZ are also observed outside the study area. They are found to be helpful to understand the lithological heterogeneity in the KMF zone and to identify various radar facies. In contrast to the western NHRFZ, a thick succession of Quaternary colluvial deposits are found in the north-flowing rivers in the eastern NHRFZ, in front of the ~W-striking KMF scarp. In the KMF zone, near-vertical Mesozoic sandstones are unconformably covered by the colluvio-fluvial deposits consisting of coarse-grained clast-supported gravels in the Falay river (Fig. 8d) (Chowksey et al., 2011b). Since the dielectric contrast is strong between the Quaternary deposits and underlying Mesozoic/Tertiary rocks, the GPR signals notably reflect off from the unconformable boundaries. The scarp-derived, poorly sorted colluvial deposits consisting of highly angular clast-supported cobbly pebbly gravels were observed in Falay river, indicating a very short transportation history near the KMF scarp (Fig. 8e) (Chowksey et al., 2011b). Tens of meters wide highly sheared near-vertical Mesozoic sandstones underlie the Quaternary clast-supported gravel deposits (Fig. 8f and g) (Chowksey et al., 2011b). Chowksey et al. (2011b) inferred that the colluvium was formed from the pre-existing KMF scarp comprising Mesozoic sandstones/shales, in
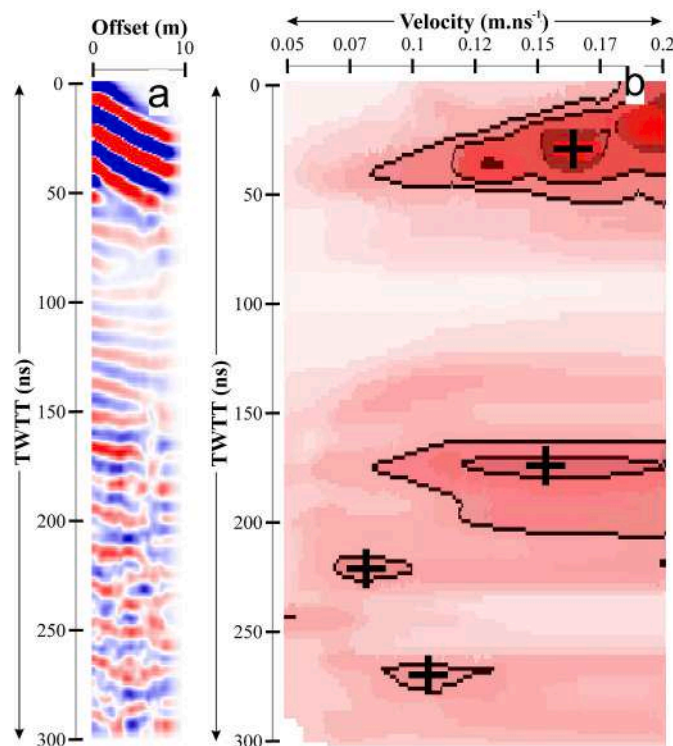
Fig. 7. Processed CMP profile and corresponding velocity diagram.

response to the neotectonic uplift along the KMF. The produced colluvial material was then reworked by fluvial agencies and redeposited over the present-day KMF, north of the paleo-KMF scarp. It is assumed that in the western part of the KMF, similar conditions still existed, but later on, they were covered by Holocene Rann sediments.

A radar facies is characterized as a zone with similar radar reflection patterns bordered by radar discontinuities (Beres et al., 1999; Jol and Bristow, 2003; Shan et al., 2015; Berton et al., 2019). Seven radar facies are identified in the study area and are described in terms of continuity and shape of reflections, amplitude response characteristics, internal reflection configuration and external package geometry (Table 2, Figs. 6 and 8h) (as per Jol and Bristow, 2003; Magalhães et al., 2017). Radar facies definition and mapping of reflections termination contribute to delineation of surfaces such as truncation, onlap and downlap (Berton et al., 2019). These erosional surfaces or depositional breaks are basically the sediment-bedrock interfaces, which are important to define the fault zone stratigraphy. The erosional surfaces picked from the radargrams appear wavy.

The depth-wise decay in GPR positive amplitude response is discussed (Figs. 6 and 8h). The radar response characteristics of different stratigraphic units were determined by picking a few GPR traces across different lithological formations from each of the processed linescan radargrams. The maximum positive radar amplitude values were computed for the Quaternary deposits, Mesozoic sandstone/shale and Tertiary limestone along the picked GPR traces. The relative amplitudes were noted at regular depth intervals. Note that during radargram processing, a linear gain function was used, which applies linear gain to the entire data set while leaving relative amplitude values unaffected. With such obtained values, it is possible to divide the radargrams into radar facies: Holocene deposits into radar facies r1a-hso and r1b-hso (up to 20–30 ns), Late Pleistocene deposits into r2-lpw (between 20 and 30 ns) (Maurya et al., 2009; Khonde et al., 2011), Mesozoic sandstone/-shale into r3a-ms and r3b-ms (between 25 and 120 ns), Tertiary limestone into r4a-tl and r4b-tl (between 25 and 120 ns). Note that the radargrams were collected during different field seasons and under varied weather conditions, which could have resulted in changes in

subsurface water content in the fault zone, affecting the amplitude responses owing to permittivity contrast. However, radar amplitude analysis has effectively established a relationship between GPR amplitudes and lithological formations in the KMF zone. Fig. 8h presents the results of radar amplitude analysis. The logarithmic function is fitted with the data, which shows depth-wise decay in amplitude response. Multiple logarithmic curves can be distinguished into orange curves for the unconsolidated colluvio-fluvial Quaternary deposits (50–7000 μV amplitude range), green curves for Tertiary limestones (50–600 μV amplitude range) and blue curves for Mesozoic sandstone/shales (600–7000 μV amplitude range). The sediment-bedrock interface is generally encountered at 30–50 ns (neutral zone in Fig. 8h). Clay-rich Tertiary limestones, because of their high conductivity, produce low-amplitude responses, resulting in high attenuation. Whereas, the sand/shale dominated stratified Mesozoic siliciclastic rocks are characterized by comparatively high-amplitude responses because they serve as an excellent dielectric medium. The Quaternary colluvial deposits are marked by moderate-to high-amplitude responses and the deposits range from poorly sorted, matrix-supported deposits to moderately sorted, pebbly clast-supported deposits (Chowksey et al., 2011a; 2011b). This general outline was used for radargram interpretation and to distinguish the radar stratigraphy, which was supported by the field observations.

5.6. GPR attribute analysis

To strengthen the discontinuities identification and interpretation, the radargrams were further processed with Hilbert transform using the envelope attribute (instantaneous amplitude) and instantaneous phase attribute (Ercoli et al., 2015) (Fig. 6). The envelope display is useful for illustrating the energy reflected from the subsurface strata. Envelope (instantaneous amplitude) calculates the absolute value of each wavelet by converting negative wavelets to positive wavelets, resulting in a positive mono-pulse wavelet. This process was used by observing the signal strength and reflectivity contrast to detect the energy loss that happens, in some cases, when a highly deformed fault zone is
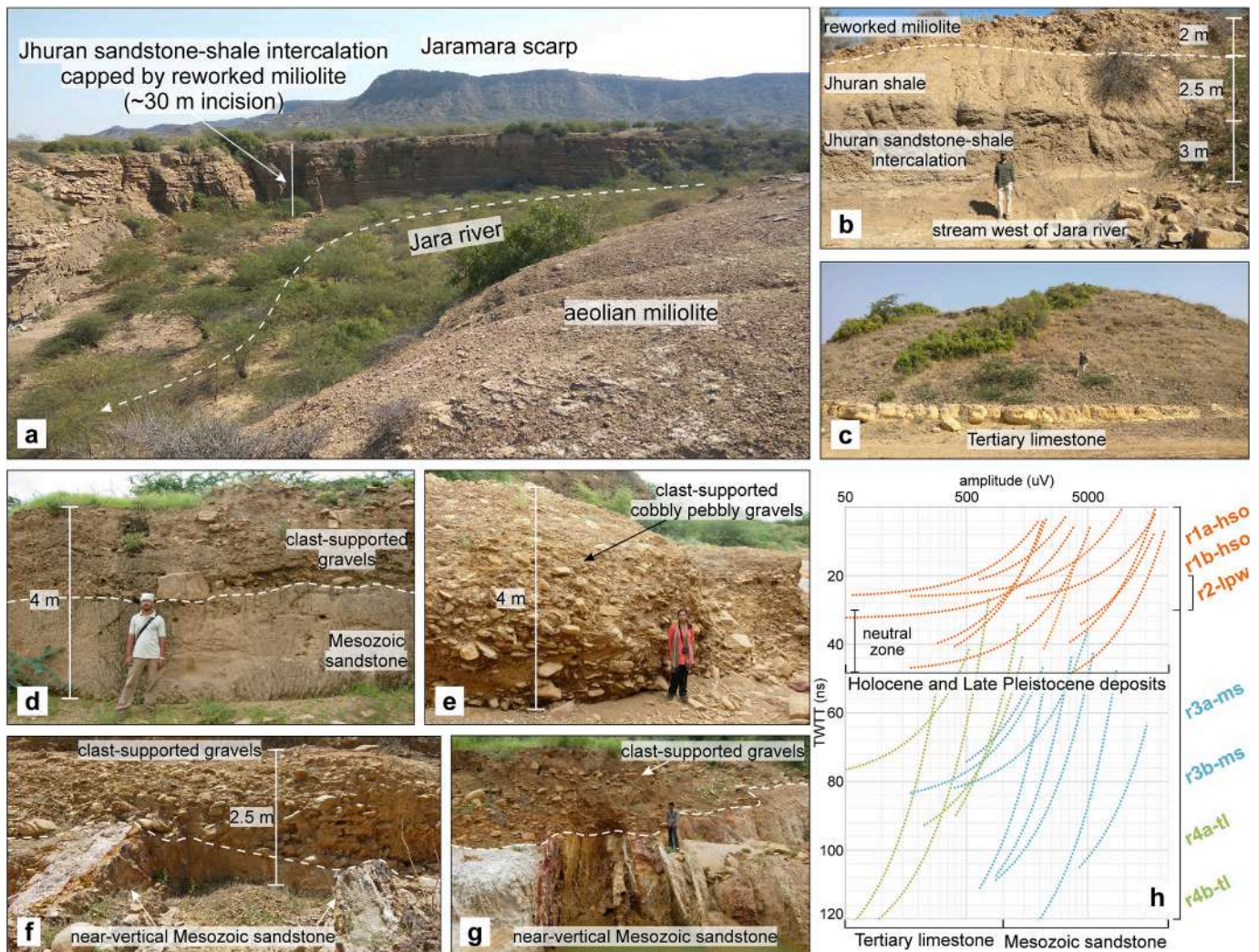
Fig. 8. (a) View of the Jara river facing south, at the southern margin of the Jara dome. (b) ~7.5 m high incised cliff of a stream west of Jara river. Thin-bedded Jhuran sandstone-shale intercalation is capped by 2 m thick colluvio-fluvial miliolite deposits. (c) A mound of Tertiary limestone in the vicinity of the Karanpur dome. (d) ~4 m high river cliff section exposing thick clast-supported gravels resting unconformably over undeformed Mesozoic sandstones. (e) ~4 m high Falay river section comprising coarse, angular clast-supported gravels. (f) and (g) Clast-supported gravels resting unconformably over near-vertical, deformed Mesozoic sandstones in Falay river. (h) Plot showing depth-wise decay in radar amplitude responses. The upper logarithmic axis represents radar amplitude in uV, while the left axis represents two-way travel time (TWTT) in ns. Orange curves for Holocene and Late Pleistocene deposits, green for Tertiary limestones and blue for Mesozoic sandstones/shales. (For interpretation of the references to color in this figure legend, the reader is referred to the Web version of this article.)

encountered in the radargrams. The energy loss in the envelope attribute is determined by the seasonal weather changes and physical properties of the fault zone, such as conductivity (Nobes and Hornblow, 2021). The results were more sensitive to detect the fault plane/zone based on envelope attribute rather than amplitude information. The use of trace envelope superimposition over wiggle trace radargrams has greatly enhanced the subsurface morphostratigraphic and structural interpretation (Cinti et al., 2015). The abrupt truncation of high-magnitude contours often suggests the occurrence of subsurface discontinuity in the envelope attribute. Across the discontinuity, the high energy regions do not persist. The instantaneous phase attribute gives equal strength to weak and strong reflections and thus emphasizes the discontinuity of reflections. The instantaneous phase attribute can be used to denote the lateral continuity of the subsurface litho-units. Abrupt changes in the phase attribute, therefore, highlights the presence of a subsurface discontinuity. The phase information is useful in delineating structural and stratigraphic features viz., faults, onlaps and prograding reflections.
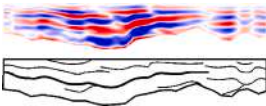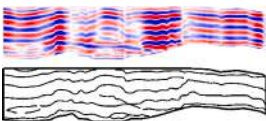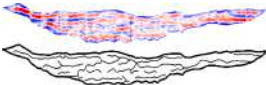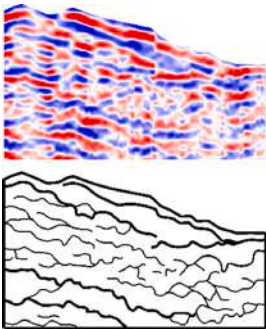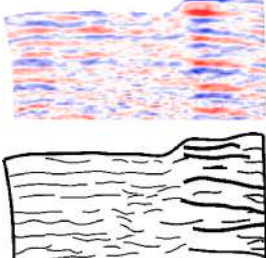
6. GPR interpretation

Depending on the GPR antenna frequency and profiling orientation, the heterogeneity of the fault material, subsurface sediment permittivity and width of the fault damage zone, major and subsidiary faults geometry generate a variety of radar signatures (Green et al., 2003 and references therein). Keeping these points into account, each radargram and its attributes are thoroughly analyzed. By verifying the interpreted radargrams with the exposures of KMF wherever available, radar facies signatures of all survey sites are characterized. The radar facies characterization and its integration with amplitude pattern/strength and multiple attribute analysis help to qualitatively infer the conductivity of subsurface sedimentary units.

The radargrams collected from five survey sites along the KMF are discussed (Fig. 2). For a detailed representation of the geophysical character of radar data, the display format varies between *(i)* linescan radargram, *(ii)* wiggle traces overlapped by envelope attribute, *(iii)* phase-based attribute and, *(iv)* interpreted sketch. The raw radargrams were 40–50 m long, but only an interesting portion from each radargram is presented for a higher vertical resolution. In all the cases, the fault
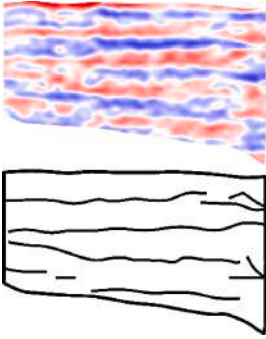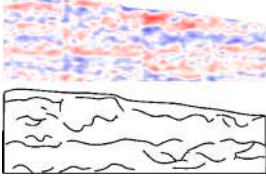
Table 2

Summary of radar response characteristics and corresponding geological interpretation. Terminology of radar facies is based on the amplitude response pattern, continuity and geometry of radar reflections and lithology type.

Radar facies code	GPR example and interpretation	Reflectors pattern	Reflectivity characteristics	External form	Relative amplitude	Geological interpretation
r1a-hso		Thick persistent, sub- wavy, horizontal/ horizontal and undeformed reflectors.	Always observed in the uppermost parts of GPR sections (E.g., Site 1: Fig. 9). It becomes thicker towards north in the Great Rann. No internal bounding surface. Lateral extent is tens of meters. r1-hso marks the top of radargrams. Occasionally affected by subsidiary faults with normal slip-sense.	Elongated	Moderate to high amplitude	Thin Holocene soil (hso) representing surficial loose Rann sediments. Represented by blue color in Fig. 14d.
r1b-hso		Wavy to sub-horizontal, continuous, parallel reflections. Occasionally wavy reflections.	Internal bounding surface present. Width of r1b-hso is tens of meters. r1b-hso is separated from r1a-hso by the conformable surface. Marks the sediment-bedrock interface in the footwall of KMF.	Elongated	High amplitude	Holocene soil (hso). Represented by blue color in Fig. 14d.
r2-lpw		Semi-continuous to chaotic, sinusoidal clinoforms.	They are marked by low energy zone in the magnitude envelope (E.g., Site 2: Fig. 10). Concave-up geometry, which is tapering on both sides along the subsidiary slip planes. Horizontal length of ~25 m. Well-defined internal bounding surfaces. Reflectors downlapping on to the disconformable contact.	Wedges delimited by erosional surfaces.	Moderate to low amplitude	Late Pleistocene colluvial wedge (lpw) deposits, which downlap on to the disconformable contact. E.g., Fig. 4e and uppermost units in Figs. 6i, j, k. ~4 m thick clast-supported cobbly pebbly gravels are shown in Fig. 6l. Represented by orange color in Figs. 14b–d.
r3a-ms		Semi-continuous, Gentle to moderately dipping reflectors.	Separated from overlying Late Pleistocene deposits by the unconformable surface. Well-represented in Fig. 10 (Site 2). Occasionally, oppositely dipping converging reflectors pattern (20–30° dip) is found. No internal bounding surface. Downlapping reflections are also observed. Located towards the footwall of the KMF.	Undefined	Moderate to high amplitude	Mesozoic clastic, fine to coarse-grained sandstone/shale (ms) lithology. E.g., Figs. 4l and n.
r3b-ms		Disrupted, irregular, deformed reflections with little or no continuity.	R3b-ms is well-represented in Fig. 11 (Site 3). Parallel termination. No internal bounding surface. Located towards the footwall of the KMF.	Undefined	Low amplitude	Attenuated energy comes from the massive, deformed deposits of Mesozoic sandstone/shale (ms) rich lithology.

(continued on next page)

Table 2 (*continued*)

Radar facies code	GPR example and interpretation	Reflectors pattern	Reflectivity characteristics	External form	Relative amplitude	Geological interpretation
r4a-tl		Broken, chaotic/sub-horizontal reflections.	Parallel termination, which is well-represented in Fig. 13 (Site 5). Laterally transform into r4b-tl or be terminated by the tectonic contact. Lack of any internal bounding surface. Located towards the hangingwall of the KMF.	Undefined	Reflection-free or faint reflections in few cases.	Clay rich, highly compacted, deformed Tertiary limestone (tl) deposits. E.g., Figs. 4i, j and 6g, h.
r4b-tl		Chaotic/semi-continuous, horizontal to sub-horizontal reflections.	Parallel termination (E.g., Site 4: Fig. 12). Lack of any internal bounding surface. Separated from r4a-tl with the presence of an erosional surface. Located towards the hangingwall of the KMF.	Undefined	Bright amplitude	

zone has been interpreted by observing the radar signatures such as, the abrupt lateral change in amplitude, sudden truncation of reflections, regions with high energy loss (high signal attenuation) that are well-recognized criteria for detecting faults with lithological contrast (McClymont et al., 2008a, 2008b; Shaikh et al., 2020). Based on variation in radar reflection patterns, the radargrams are divided into several zones of distinct radar facies (detailed in sub-sections 6.1–6.5). Much of the radar facies interpretation is based on the surficial field observations and Quaternary stratigraphic units exposed in the study area or along the eastern part of the KMF (detailed in sub-section 5.5). Because of the significant difference in the composition of Mesozoic and Tertiary rocks, the radar signatures of both the rock types exhibit large variance across the KMF. The radargrams presented have no obvious vertical exaggeration and, the reflections may not show true dip as the steep reflections may have been affected by any migration algorithm applied in the processing flow.

Because the KMF zone is highly brittle deformed, it is profoundly impacted by multiple near-vertical north-dipping synthetic/south-dipping antithetic discontinuities with notable slip. Most of the slip planes are confined to the upper parts of the radargrams. Also, they are all well-supported by the GPR attribute interpretation. In the western part of the KRB, It is important to understand the relationship between the subsidiary slip planes and the general structural pattern of the KMF. The upper few meters of all the radargrams are occupied by Quaternary deposits. In the study area, the Quaternary deposits comprise base-of-scarp colluvial deposits, valley-fill miliolite and alluvium, which have been eroded from the KMF scarp and deposited in the footwall (Chowksey et al., 2010). Thus, the GPR surveys allowed us to verify the thickness and depositional pattern of the Quaternary sediments across the KMF, mainly along the downthrown block.

6.1. Site 1

Site 1 is located SE of Karanpur dome, at the westernmost part of study area (Figs. 2 and 9). Eocene nummulitic limestones (N105° strike, N15° dip direction and 85° dip) and highly-sheared near-vertical Mesozoic sandstone crop out near survey site. The contact between the Mesozoic and Tertiary rocks marks the surface position of the NNW-striking KMF (Fig. 4h). A 22 m long GPR transect was conducted in

N40° orientation crossing the litho-tectonic contact near-perpendicularly. The paleo-morphological scarp at the survey site could have been eroded, leaving a flat topography behind and, therefore, there was no need to compensate for the elevation differences in the radargram.

The radargram shows a distinct radar reflection pattern and contrasting amplitude strength across the KMF (indicated by black arrows in Fig. 9a). The radargram depicts the following radar facies: *(i) r3a-ms.* On the SW side, between ~20 and 95 ns, continuous high-amplitude thick reflections are observed, which correspond to the highly-compacted Mesozoic sandstone located in the upthrown block of the KMF (marked by dark green lines in Fig. 9d). The envelope attribute in Fig. 9b shows high energy contours corresponding to the Mesozoic sandstones. *(ii) r4a-tl and r4b-tl.* Chaotic, moderate–low amplitude (or reflection-free) r4b-tl indicate *(a)* massive, structureless, homogeneous lithology, *(b)* high amount of clay content in limestones that attenuate the GPR signals. In the NE side, comparatively, weak amplitude signal returns with a successively increasing dip characterize r4a-tl of Tertiary limestone. The envelope attribute denotes scattered, low energy contours of r4a-tl and r4b-tl as compared to high energy contours of r3a-ms. *(iii) r1a-hso.* Semi-continuous low–moderate amplitude r1a-hso characterizes the Holocene valley-fill deposits unconformably capping the older rock sequence. *(iv) r2-lpw.* The r2-lpw encompasses a semi-continuous to chaotic reflections pattern as it encloses the low amplitude zone. This represents a colluvial wedge-out geometry, which comprises Late Pleistocene valley-fill deposits e.g., miliolitic sands, scree deposits, conglomeratic boulders, coarse sandy material etc. The jumbled up material will essentially give a chaotic reflection pattern that lacks sedimentary layered stratification. Thinning of sediments on both sides from the central part, covering the entire length of the upper section of the radargram, indicate that the colluvial wedge dies away from the main strand. The envelope attribute clearly defines the tapering geometry of colluvial wedge. The warping of reflections of r1a-hso and r2-lpw can be observed between 5 to 10 m distance, which are also marked by high energy contours in envelope attribute.

6.1.1. Tectonic interpretation

Nearly 5–7 m wide low amplitude anomaly, mostly occupied by r4b-tl, indicates the presence of the fault zone. The subsurface presence of
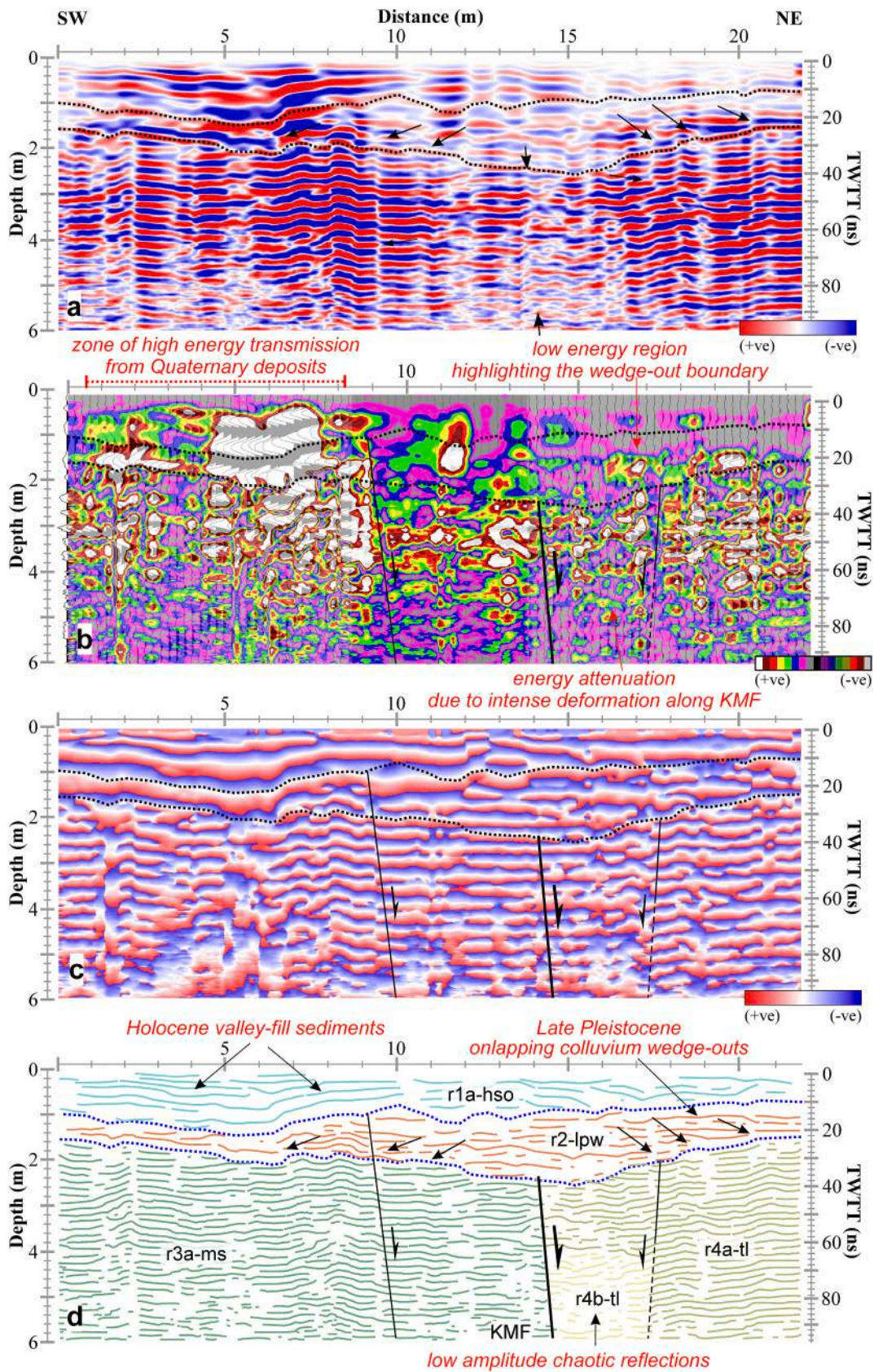
(caption on next page)

Fig. 9. 22 m long, NE-oriented radargram acquired across the KMF over a flat soil surface, between Karanpur dome and western flank of Ghuneri dome at site 1. See geological map of the study area in Fig. 2 for the location of GPR survey site. Axis on left side shows penetration depth in meters and on right side two-way travel time (TWTT) in ns is denoted. The upper axis shows section length in meters. (a) Interpreted linescan radargram. GPR amplitudes are represented by red (positive) and blue (negative) reflections. Arrows indicate the projected location of the KMF and interpreted position of secondary synthetic and antithetic slip planes. Black wavy dotted lines indicate conformable and non-conformable contacts between individual lithounits. (b) Envelope attribute draped over wiggle traces. The color scale reflects the energy continuum, with white contours representing the highest energy regions, while the lowest energy regions are represented by grey contours. The lateral energy changes of EM waves marks the presence of fault planes. (c) Trace envelope based on phase attribute. (d) Interpreted sketch with lithology represented by colored lines. From top to bottom, based on the reflections response pattern, the radargram is divided into radar facies r1a-hso: uppermost Holocene Rann sediments, r2-lpw: Late Pleistocene colluvial wedge-outs, r3a-ms: Mesozoic sandstone, r4a-tl and r4b-tl: Tertiary limestone. Note the presence of wedge-shaped deposits with onlapping and pinch over reflections that terminate against the disconformable sediment (r2-lpw)-bedrock (r3a-ms and r4a-tl) interface. Black lines indicate fault planes and half-arrows denote movement direction of the upthrown block in Figs. (b–d). The KMF with normal slip can be appreciated due to strong attenuation contrast and clear lateral discontinuity of the reflections between 13 and 15 m distance. Note the offset of continuous reflections in r3a-ms and r4a-tl, and correspond to secondary normal synthetic and antithetic slip planes. (For interpretation of the references to color in this figure legend, the reader is referred to the Web version of this article.)

the KMF is marked by: *(i)* truncation and abrupt amplitude decrease of r3a-ms and r4b-tl. *(ii)* Envelope attribute highlights poor reflection events, high signal attenuation (Lacan et al., 2012). The relatively "transparent" zone indicates extreme energy loss in the KMF zone due to intense deformation or the presence of clay-rich lithology. The discontinuity of r3a-ms along the KMF can be observed in the instantaneous amplitude attribute. *(iii)* The colluvial wedge, which is the compelling proof to assess the presence of the KMF. The colluvial wedge might have collapsed from the paleo-KMF scarp, which has now been eroded. It is inferred from the radargram that the KMF is a steep NE-dipping normal fault at the SE of Karanpur dome. The KMF does not propagate upwards into the Holocene (r1a-hso) and Late Pleistocene (r2-lpw) deposits. However, the surficial exposure of the KMF partially covered by tilted miliolite deposits, located in the close vicinity of the survey site, testifies the KMF to be neotectonically active (Fig. 4d and e). The slip planes are exposed in r3a-ms and r4a-tl and, of them, the NE-dipping synthetic normal slip plane at ~9 m distance displaces r2-lpw. The SW-dipping antithetic normal slip plane at ~17 m distance marks truncation of r4a-tl.

6.2. Site 2

It is located between Ghuneri dome and Mundhan anticline, near Sahera, where the strike of the KMF switches to NNW (Figs. 2 and 10). The change in the strike may be due to the oblique-slip motion along a ~NW-striking GUF, which end up in the deformation zone of the KMF (Figs. 2 and 5e). The highly deformed compacted Mesozoic sandstones crop out in patches at the southern side while the unconsolidated reddish clay-rich Tertiary limestones crop out at the northern part of the transect line. The transect runs almost perpendicular to the KMF strike and parallel to a nearby small river channel.

The characteristics of each of the radar facies are discussed below. *(i) r1a-hso, r1b-hso and r2-lpw.* The geometry and reflection patterns of r1a-hso, r1b-hso and r2-lpw at site 2 (Fig. 10) are quite different from those observed in radargrams recorded across the KMF near Lakhpat anticline and Karanpur dome (site 1: Fig. 9). This variance in the radar response characteristics may be attributed to different processing parameters utilized during survey operation and also, the acquisition of radargrams were made during different field seasons. The uppermost black dotted horizontal line at < 1 m depth, represents the conformable contact between the youngest surficial loose soil sediments (r1a-hso) and underlying Holocene deposits (r1b-hso) (Fig. 10d). The r1a-hso, r1b-hso and r2-lpw occupy upper 2–3 m depth overlying the disconformable sediment-rock contact (blue wavy dotted line in Fig. 10d). Since the reflections above and below the disconformity do not show much variation in dip, the contact cannot be a bounding surface. The r2-lpw is located towards the footwall and plausibly truncated by the KMF towards north. The r2-lpw is defined by concave-shaped geometry with a horizontal length of ~25 m, resting over the r3a-ms and r3b-ms (deformed Mesozoic sandstones). Semi-continuous to chaotic reflections of r2-lpw emerges from Late Pleistocene channel-fill deposits,

which along the slip planes are tapered on both sides. The low amplitude zone of r2-lpw can be readily demarcated in the envelope attribute (Fig. 10b). The r2-lpw shows downlapping reflections on to the sediment-bedrock unconformable surface, which indicates a localized progradational pattern (Shan et al., 2015). Below the disconformity, r3b-ms show poor magnitude response due to the highly deformed zone. Note that no subsidiary strand offsets r2-lpw except normal slip plane at ~5 m distance.

(ii) r3a-ms and r3b-ms. On the southern side, r3a-ms exhibits oppositely dipping converging reflections pattern (20–30° dip) forming a folded geometry, which is expressed by the localized syncline. The semi-continuous reflections of r3a-ms representing the Mesozoic sandstone grade into chaotic reflections of r3b-ms representing the clastic, fine to coarse-grained sandstone. The r3b-ms exhibit high attenuation, which may have been caused by high electric conductivity, e.g. due to high clay content in Mesozoic rocks (Grützner et al., 2012) (Fig. 10d). *(iii) r4a-tl and r4b-tl.* Towards the northern side, in the hangingwall, r4a-tl and r4b-tl represent Tertiary limestones. The contact zone (30–50 ns depth) of Tertiary limestones and overlying Holocene alluvium exhibits flat bright amplitude reflections of r4b-tl tapering towards north. Clay-rich, highly compacted Tertiary limestones caused contortion of radar signals from the lower parts, resulting in poor reflectivity and broken reflections of r4a-tl (Grützner et al., 2012).

6.2.1. Tectonic interpretation

Approximately 88° north-dipping KMF with normal slip-sense is inferred at ~29 m distance by observing abrupt phase change in amplitude of r3a-ms. The r3a-ms shows wide amplitudes cycles whereas r4a-tl and r4b-tl show narrow and weak amplitude cycles (Fig. 10a, c). The reflections also die out at the main fault strand. The KMF also extends upward into Late Pleistocene and Holocene deposits. The envelope attribute substantiates the presence of KMF as the high energy contours of r3a-ms terminate against the KMF, which continue as low energy contours of r4a-tl and r4b-tl in the hangingwall (Fig. 10b). Because of the prevalence of compressive stress regime and structural complexities in the deformation zone of the KMF, multiple normal slip planes were recognized. The subsidiary strands display: *(i)* displacement of semicontinuous to broken, contorted reflections, *(ii)* warping and truncation of continuous reflections, and *(iii)* an amplitude variation across slip planes. Their position is also supported by the envelope attribute as an abrupt lateral transition in the energy pattern happens across slip planes (Fig. 10b). None of the slip planes penetrate upwards into r1a-hso, r1b-hso and r2-lpw. Above the disconformity, however, a south-dipping normal slip plane is displacing the r1a-hso at 31 m distance. In proximity to the KMF, another near-vertical discontinuity is identified at ~27 m distance. This indicates that the majority of slip planes remained inactive during the Quaternary at site 2.

6.3. Site 3

Site 3 is located near eastern flank of the Jara dome (Figs. 2 and 11).
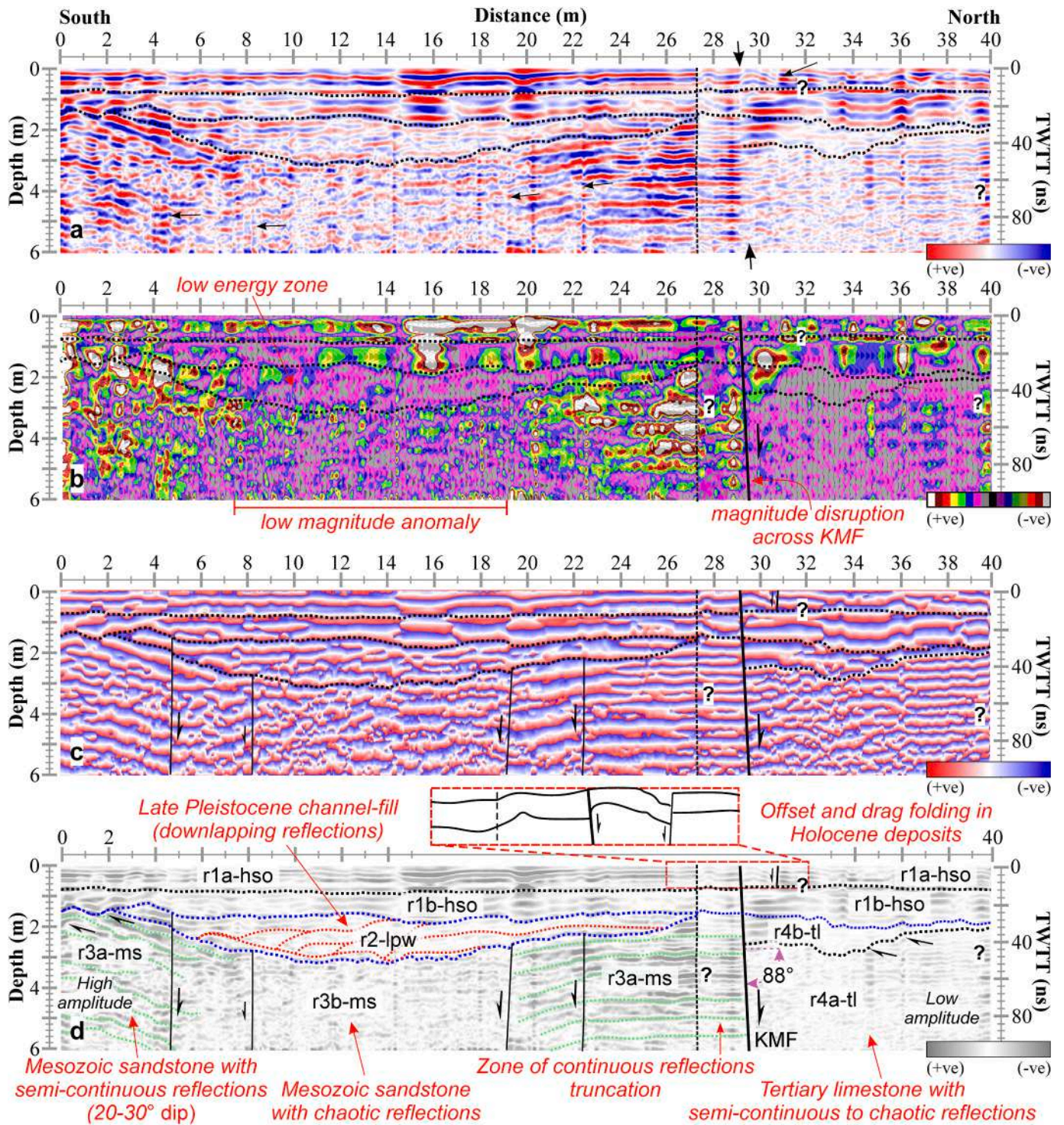
Fig. 10. (a–c) as for Fig. 9(a–c) but for the radargram recorded across the KMF, near Sahera at site 2. See geological map of the study area in Fig. 2 for the location of GPR survey sites. (d) Interpreted grayscale radargram. The hangingwall of the KMF is towards north and footwall is towards south. From top to bottom, based on the reflections response pattern, the radargram is divided into radar facies r1a-hso and r1b-hso: Holocene deposits, r2-lpw: Late Pleistocene channel-fill deposits with tapering geometry and downlapping reflections, r3a-ms and r3b-ms: Mesozoic sandstone with chaotic reflections, r4a-tl and r4b-tl: Tertiary limestone.
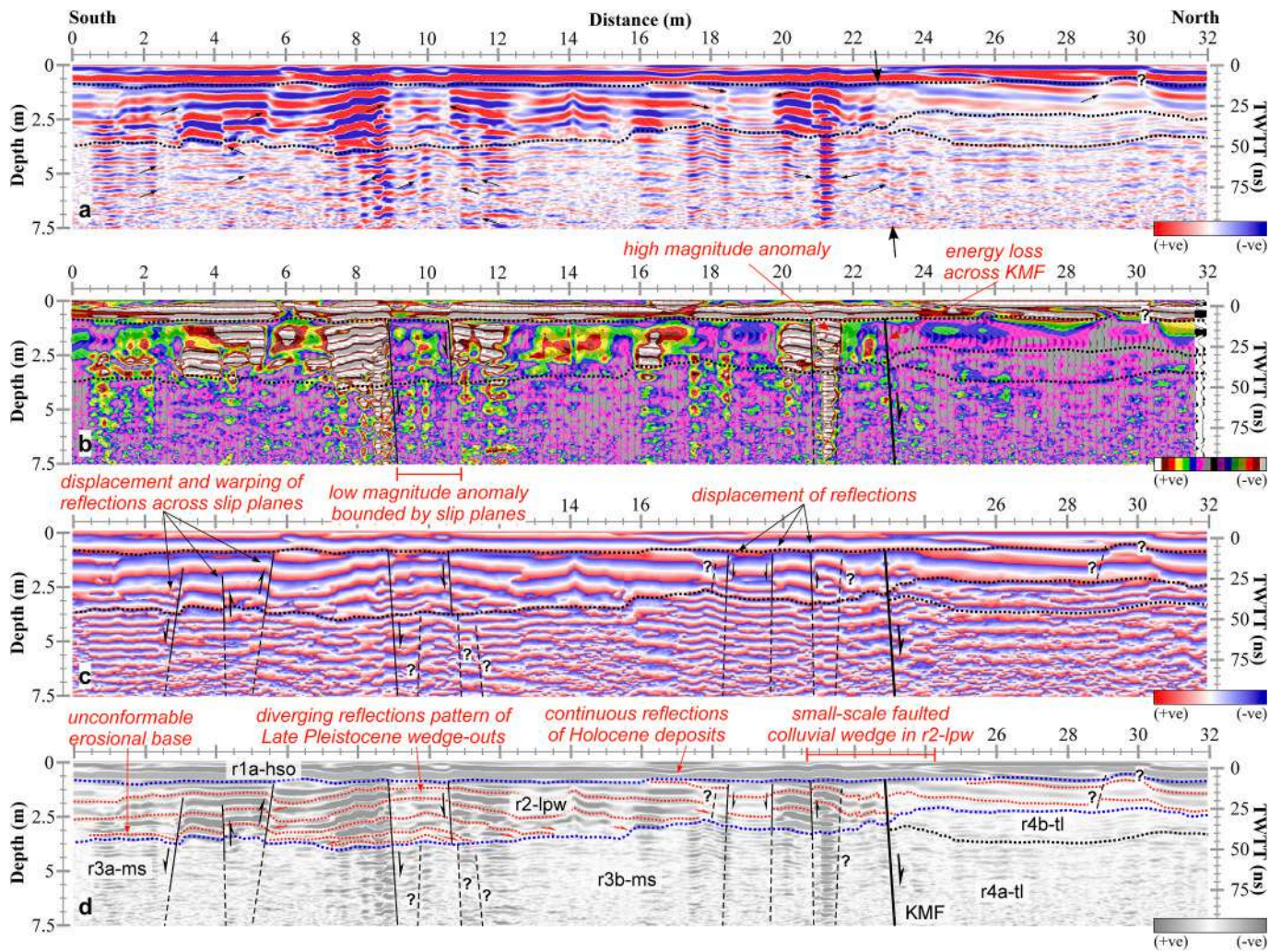
Fig. 11. (a–d) as for Fig. 10(a–d) but for the radargram recorded across the KMF, near eastern flank of the Jara dome at site 3. See geological map of the study area in Fig. 2 for the location of GPR survey sites. The question marks in Fig. (d) suggest possible slip planes with indeterminate kinematics that are not identified in the radargram using the absolute criteria for fault plane marking. However, a couple of low amplitude r2-lpw reflections appear to offset along the potential slip plane at 29 m distance. The question mark at 30 m distance denotes the possibility of Late Pleistocene deposits bulging locally (r2-lpw).

The GPR surveys at sites 3, 4 and 5 were conducted on a flat Great Rann surface and a few tens of meters north of the gentle to steep north-dipping scarp of the Jara dome, inter-domal saddle occupied by the Ukra intrusive and Jumara dome respectively (Fig. 2). The KMF is certainly not located at the base of scarp. Because of a prolonged denudation, the fault scarp has experienced continuous retreat and therefore, the actual trace of the KMF is located further north of the base of scarp, buried below the Great Rann surface.

The following radar facies were interpreted: *(i)* Thickest Late Pleistocene colluvial wedge with a maximum thickness of ~2 m is represented by r2-lpw (Fig. 11). The footwall develops a high amplitude bidirectional wedge-out geometry, but the hangingwall exhibits a relatively flat low amplitude reflections (Fig. 11a). This is also validated from the envelope attribute (Fig. 11b). The vertically stacked aeolian sheet miliolite deposits may have generated r2-lpw. Such phenomenon can be comparable with titled miliolite deposits above the lithotectonic contact of the KMF, at the eastern fringe of the Karanpur dome (Fig. 4d and e). The r2-lpw get increasingly narrower until it wedges-out towards north. It forms a lobe-shaped geometry with diverging and gently dipping reflections, implying that the beds are downlapping on to the unconformable surface towards both north and south directions. At ~10 m distance, in the central part of the lobe-shaped structure, thickening of reflections can be observed, while thinning can be observed in both

directions away from the central part. These characteristics suggest that the transect line was perpendicular to r2-lpw with a lobe-shaped geometry. High amplitude, long, continuous r1a-hso of Holocene deposits conceals the colluvial wedge.

(ii) r3a-ms and r3b-ms. Semi-continuous reflections of r3a-ms located between 0 and 8 m distance, grade into chaotic reflections of r3b-ms between 12 and 16 m distance. *(iii) r4a-tl and r4b-tl.* In the hanging-wall, r4a-tl shows poor reflectivity from clay-rich Tertiary limestones. Bright amplitude, flat reflections of r4b-tl tapers towards the KMF, located in the contact zone (30–50 ns depth) between r4a-tl and overlying r2-lpw. The r3a-ms, r3b-ms, r4a-tl and r4b-tl in the envelope attribute are marked by low energy contours, in contrast to high energy contours of r1a-hso and r2-lpw (Fig. 11b). Sub-sections 6.1 and 6.2 detail r3a-ms, r3b-ms, r4a-tl and r4b-tl.

6.3.1. Tectonic interpretation

The high-angle north-dipping KMF with normal slip is inferred at ~23 m distance where r2-lpw shows *(i)* reflections truncation and, *(ii)* a small-scale faulted colluvial wedge geometry. Therefore, the KMF is inferred to be neotectonically active at site 3.

The radargram also confirms that the deformation zone is affected by an array of subsidiary synthetic and antithetic slip planes. Between 1 and 6 m distance, the sense of shear and sense of rotation of the
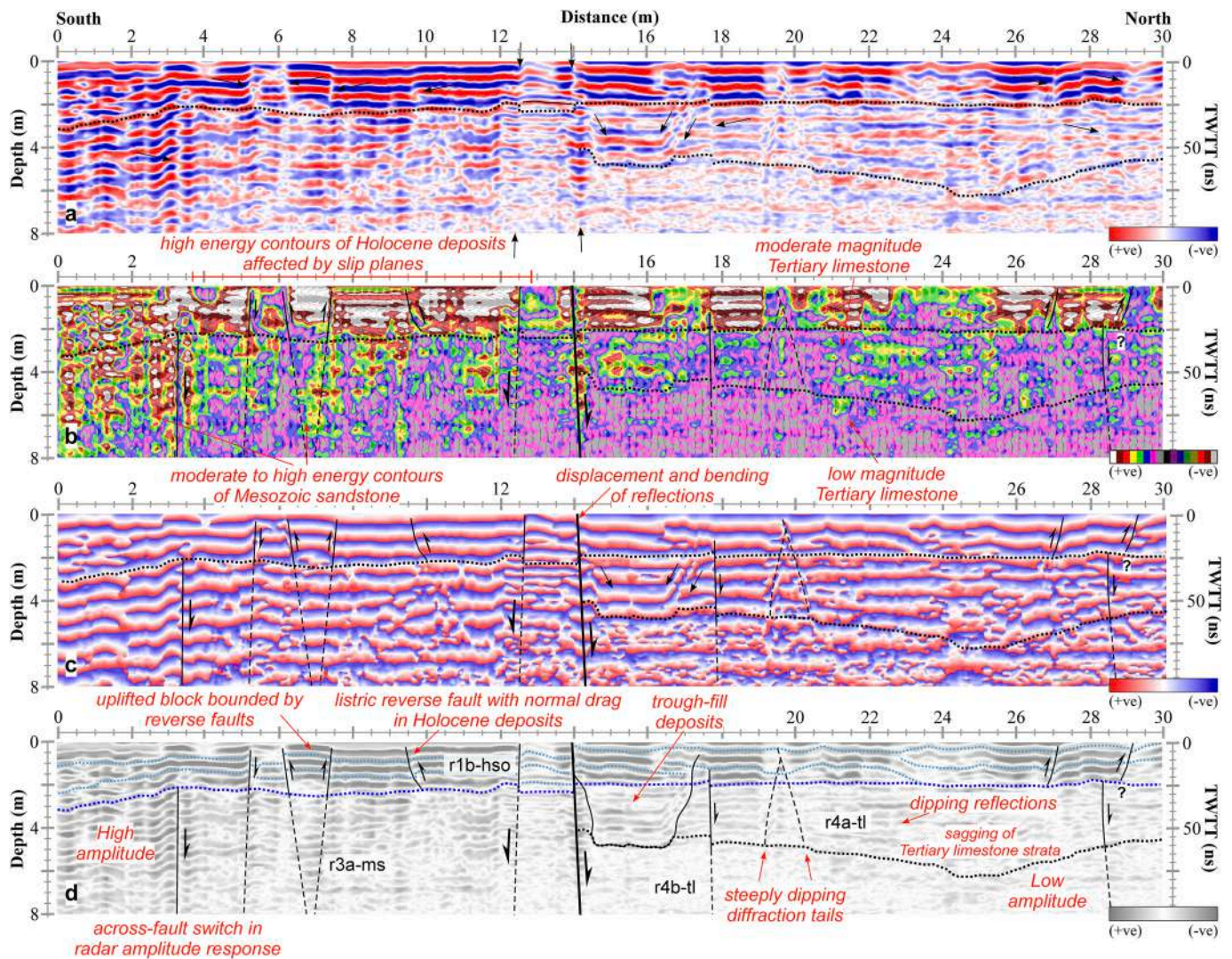
Fig. 12. (a–d) as for Fig. 10(a–d) but for the radargram recorded across the KMF, at eastern flank of the inter-domal saddle occupied by Ukra intrusive at site 4. See geological map of the study area in Fig. 2 for the location of GPR survey sites. At 20 m distance, the arrows (noise?) indicate steeply dipping diffraction tails affected by dispersion of EM waves. White regions in Fig. (d) show areas of poor reflectivity, while white contours in Fig. (b) show highest energy regions.

individual fault blocks is not the same. Normal and reverse slip planes offset r2-lpw and r3a-ms, implying their neotectonically active nature. The dip direction and slip-sense being non-uniform, the fault blocks cannot be termed accurately as "dominos" (Stewart and Argent, 2000). Slip plane at 4 m distance shows offset of reflections, while other slip planes show twisting/bending of reflections. The slip planes with inde-terminate kinematics and artifacts that show prominent radar signatures are denoted by dashed lines with a question mark in Fig. 11d.

A fault rupture during a large earthquake will certainly arrive from the hypocentre to the surface. Therefore, a fault rupture can propagate from the bedrock to the overlying Quaternary deposits, but this is not reflected in the interpreted radargram, particularly for slip planes that are constrained to r2-lpw. They may be affecting the bedrock, but due to strong attenuation by r1a-hso and r2-lpw, there are faint radar signa-tures in r3a-ms and r3b-ms.

Two distinct radar anomalies have been observed in the footwall persisted throughout the depth (data up to 7.5 m depth) of the radar-gram disturbing the Mesozoic sandstone and overlying Late Pleistocene colluvial deposits: *(i)* low amplitude anomaly at ~10 m distance and *(ii)* high amplitude anomaly at ~21 m distance. The 2 m wide low ampli-tude zone is fringed by conjugate normal and reverse slip planes. Within this low amplitude zone, several slip planes with indeterminate

kinematics are observed. The high amplitude reflections of r2-lpw at ~8 and 12 m distance abruptly transform laterally into chaotic low ampli-tude reflections at the center indicate intense tectonic deformation. High energy contours (marked by white color) in the envelope attribute on both sides of the low amplitude zone are truncated by slip planes and transform into low magnitude contours (Fig. 11b).

Around 0.5 m wide high amplitude anomaly at 21 m distance can be observed close to the KMF. This high amplitude anomaly is fringed by normal slip planes converging at depth. The high amplitude anomaly could be an artifact caused by an amplitude spike (noise), however displacement and bending of reflections along two normal slip planes rule this out. The r2-lpw shows displacement of reflections across south-dipping slip planes between 18 and 20 m distance located to the south of high amplitude anomaly. Localized sagging of reflections of r2-lpw can be observed at ~6 m distance, obstructed by a reverse slip plane to the south. However, downward bending cannot be observed below in r3a-ms. The deformation structures are less numerous in the hangingwall than those in the footwall. The off-fault folding noted in r2-lpw at ~30 m distance is accompanied by a minor south-dipping slip plane.
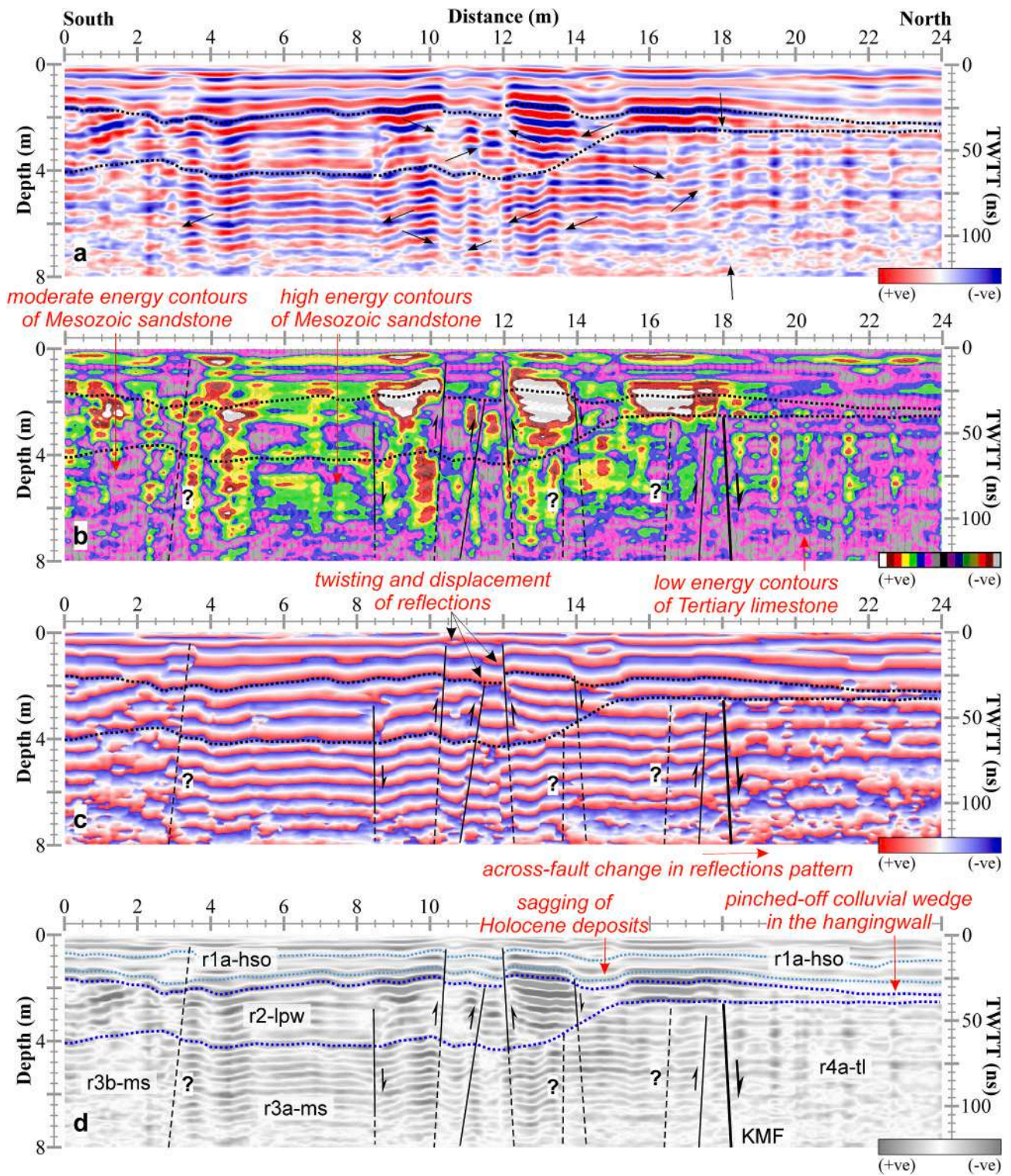
Fig. 13. (a–d) as for Fig. 10(a–d) but for the radargram recorded across the KMF, north of eastern flank of the Jumara dome at site 5. See geological map of the study area in Fig. 2 for the location of GPR survey sites.

6.4. Site 4

Site 4 is located at eastern flank of the inter-domal saddle occupied by Ukra intrusive (Figs. 2 and 12). The radar facies observed are described below. *(i) Continuous r1b-hso.* The uppermost dotted line at ~2–3 m depth, represents the disconformable contact between the Holocene deposits (r1b-hso) and underlying Mesozoic sandstone (r3a-ms)

and Tertiary limestone (r4a-tl) (Fig. 12). The high-amplitude zone of r1b-hso can be demarcated in the envelope attribute as high-energy contours (Fig. 12b). *(ii) r3a-ms.* To the south, r3a-ms exhibits high-to-moderate-amplitude, wavy to sub-horizontal reflections. *(iii) r4a-tl and r4b-tl.* r4a-tl is in disconformable contact with the overlying r1b-hso. Sub-sections 6.1 and 6.2 details r3a-ms, r3b-ms, r4a-tl and r4b-tl.

6.4.1. Tectonic interpretation

Steep north-dipping KMF with normal slip is inferred at ~14 m distance based on radar signatures: *(i)* conversion of strong amplitude cycles of r3a-ms into weak and narrow amplitude cycles of r4a-tl and r4b-tl (Fig. 12a), *(ii)* disruption and displacement of reflections of r3a-ms along the KMF, *(iii)* bending or twisting of reflections along the KMF and, *(iv)* termination of high energy contours of r3a-ms along the KMF in the envelope attribute (Fig. 12b).

The planar and listric reverse slip planes are mainly localized in Holocene deposits (r1b-hso). The reflections are displaced with distinct change in the dip (sub-horizontal to moderate dip). High energy contours in pockets in Holocene deposits are delimited by these slip planes (Fig. 12b). The normal slip plane inferred at 3 m distance, which do not propagate upward into r1b-hso, show *(i)* displacement of reflections and, *(ii)* abrupt change in radar amplitude response. Contrarily, no amplitude change is observed along south-dipping steep normal fault at ~13 m distance. Along this slip plane, r3a-ms do not show any radar signatures, but the overlying r1b-hso show warped reflections, which suggest smalls-scale fault-related folding. Another steep normal slip plane is inferred at ~17 m distance, displacing reflections of r4a-tl and the disconformable contact.

Continuous sub-horizontal reflections are greatly displaced within the upper part of the hangingwall in the vicinity of the KMF, forming a deformed fault-related Quaternary channel-fill deposits. In a close-view, trough-fill structure shows concave-up internal reflections. Along the boundary, the trough geometry is bounded by moderate amplitude basal concave-up reflections, where offset of reflections is noticeable. This may characterize the isolated distributary north-flowing channel obstructed by the neotectonic activity along the KMF (Magalhães et al., 2017). The concave filling is related to the sedimentation governed by the tectonic movement along the KMF.

Small-scale north- and south-dipping reverse listric faults restricted to the upper Holocene deposits are the characteristics of this radargram. The radargram from no other site show listric faults. At 10 m distance, reverse listric fault with normal drag is observed as the reflections in the hangingwall are convex-up as compared to the flat reflections in the footwall (Mukherjee, 2014). At 5 m distance, the uplifted block bounded by small-scale reverse faults is observed in the Holocene deposits. Due to sediment compaction (Dasgupta and Mukherjee, 2020) of uppermost Holocene Rann sediments representing the r1b-hso, such secondary listric faults probably existed in the fault zone.

6.5. Site 5

Site 5 is located tens of meters north of eastern flank of the Jumara scarp (Figs. 2 and 13). South-dipping beds were noted at site 5, however, no such dip of radar reflections was observed in the radargram. The observed radar facies are as follows. *(i) r1a-hso.* It is characterized by long, continuousmoderate amplitude reflections representing the topmost Holocene sediments cover. Their continuity is also expressed by almost elliptical contours in the envelope attribute. *(ii) r2-lpw.* The potential colluvial wedge defined by moderate to low amplitude semi-continuous r2-lpw are thickest (~2 m) towards the footwall, which, when approaching the hangingwall, pinches-off. The wedge is more undulatory and the exact explanation why its thickness is greater in the hangingwall is to be studied, whereas thinning is observed towards north in the footwall. *(iii) r3a-ms and r3b-ms.* On the southern margin, r3b-ms is observed to exhibit low amplitude, chaotic reflections, which laterally transform into semi-continuous high-amplitude reflections of r3a-ms. The r3a-ms and r3b-ms radar facies represent Mesozoic sandstone. *(iv) r4a-tl.* Low-amplitude chaotic r4a-tl represent Tertiary limestone.

6.5.1. Tectonic interpretation

At ~18 m distance, steep north-dipping KMF with normal slip is inferred. No major displacement, bending or twisting of continuous

reflections is observed across the KMF. The amplitude response is also uniform across the KMF. There is, however, a major difference in the pattern of reflections, which marks the KMF. Semi-continuous high amplitude reflections of r3a-ms convert laterally into low amplitude chaotic reflections of r4a-tl. The envelope attribute also supports the interpretation as high energy contours of Mesozoic sandstone terminate along the KMF. The KMF does not penetrate upwards into r1a-hso and r2-lpw.

Largely, the reflections of r1a-hso are continuous and undeformed, but, at 10–12 m distance window, they are affected by subsidiary reverse slip planes. The slip planes twisted the reflections of r1a-hso. The slip planes also displace the conformable contact between r1a-hso and r2-lpw. In r2-lpw, intense zone of shearing is observed between 8 and 15 m distance. The normal and reverse slip planes that post-date the generation of colluvial wedge caused small, broken reflections in this zone. Few slip planes are marked by the displacement on the order of one amplitude cycle. On the other hand, the reflections are clearly warped in a few cases.

The lateral continuity of chaotic reflections of r3b-ms is hindered at ~3 m distance by the slip plane with indeterminate kinematics. The slip plane is marked only on the basis of the abrupt lateral shift in the reflections pattern with no displacement of reflections. Across the slip plane, the chaotic reflections (r3b-ms) convert into semi-continuous reflections with high amplitude (r3a-ms). This slip plane penetrates upwards and also disturbs r1a-hso and r2-lpw. The almost horizontal continuous reflections of r3a-ms continue up to the normal slip plane at ~8 m distance. Beyond this slip plane, semi-continuous reflections of r3a-ms transform into wavy, broken, reflections between 8 and 14 m distance. This zone of r3a-ms is affected by normal and reverse slip planes indicating highly deformed Mesozoic sandstone. The presence of slip planes is also marked by small oval-shaped contours in the envelope attribute. At ~14 m distance, the broken reflections of r3a-ms again transform into semi-continuous reflections.

7. Discussion

The seismically active NNW- to W-striking near-vertical KMF is one of the major intra-basinal faults in the KRB (Biswas, 1993) (Fig. 1). The KMF is displaced obliquely by the transverse faults (Fig. 5a–c, e). The W-striking transverse fault shown in Fig. 5a and b is exposed between the Ghuneri dome and Karanpur dome, while the NE-striking fault in Fig. 5c and NW-striking GUF in Fig. 5e run between the Ghuneri dome and Mundhan anticline. A series of such W- to NE-striking transverse faults in the inter-domal saddle regions and their oblique-slip movement probably produced a step-like strike of the KMF ascending towards the west (i.e. from NW–W).

GPR data reveal significant along the fault and off-the-main-fault deformation structures. In this work, GPR and field-based investigations were extensively performed to document the neotectonically active nature of the blind KMF and related deformation structures and to demonstrate the radar characteristics of the fault zone. Since the KMF is largely buried underneath Quaternary sediments cover in the western part of the KRB, there are only a few sites where across-fault GPR surveys could be performed after intensive field studies. Most of these sites exist a few tens of meters north of structural domes located on the upthrown block of the KMF. The GPR surveys were systematically planned and data were recorded where in the case of normal dip-slip motion, hangingwall and footwall comprise of Tertiary and Mesozoic age rocks, respectively. The radargrams portrayed sufficient resolution and depth of penetration ($<$~8 m, 100–125 ns TWTT) in the sediment-rock successions.

The blind KMF can be traced using GPR in terms of distance and projected to the uncovered outcrop (Fig. 4d). Thus, GPR data across the blind KMF from several locations are compared to the outcrop exposures wherever they are available. The illustrations indicate that the radargrams not only offer the ability to map blind active faults, but also help

to visualize the associated subsidiary slip planes; fault-scarp associated deformed sedimentary structures in the subsurface, viz., onlapping, tapering coarse-grained clastic colluvial wedges, truncated river channel/channel-fill deposits in the uplifted block and folded strata. Thus, the existence of the blind active faults can be linked with well-defined deformed sedimentary structures preserved in the fault zone. Therefore, high-resolution GPR can be used as a rapid and non-destructive alternate tool for pre-trenching paleoseismological studies. New GPR findings from the KMF zone in this work shed light on the slip geometry and associated structures. However, 2D radargrams alone are inadequate to determine fault orientation. This contribution also covers approaches of GPR data interpretation and ways of fault imaging.

After GPR data collection (Sub-section 5.2), the post-survey data processing (Sub-section 5.3) and interpretation (Section 6) were performed in light of field observations. The present low-relief steep north-facing topographic KMF scarp is largely the result of post-Miocene uplift (Shaikh et al., 2019). The KMF scarp delimits the rugged rocky topography of the discontinuous chain of domes located in the upthrown block. The current position of the KMF, however, is not at the base of scarp, but rather further north, buried below the flat Great rann surface. Therefore, GPR profiles were acquired on a flat rann surface starting from the scarp-base, with no topographic corrections required and hence, no topographic scarps are visible in the radargrams.

Comprehensive GPR reflection amplitude analysis and field observations of river cliff sections were found critical for estimating various radar facies (Sub-section 5.5, Fig. 8). To deduce potential subsurface fault zone stratigraphy, seven types of radar facies-r1a-hso, r1b-hso, r2-lpw, r3a-ms, r3b-ms, r4a-tl and r4b-tl and six types of radar surfaces-r1a-hso-r1b-hso, r1b-hso-r2-lpw, r2-lpw-r3a-ms/r3b-ms/r4a-tl/r4b-tl, r3a-ms-r3b-ms, r4a-tl-r4b-tl, r3a-ms/r3b-ms-r4a-tl/r4b-tl (lithotectonic contact) were described and compared to outcrop exposures. The KMF acts as the lithotectonic contact between the Mesozoic sandstones (r3a-ms and r3b-ms) exposed in the NHRFZ in the upthrown block and the Tertiary limestones (r4a-tl and r4b-tl) exposed in the form of thin strips in the northern downthrown block, mostly covered by a thin cover of Quaternary sediments (r1a-hso, r1b-hso and r2-lpw). Sharp amplitude contrast in between the Mesozoic-Tertiary rocks is interpreted as the result of distinct dielectric contrast on account of deformation along the KMF. The hard, well-compacted Mesozoic sandstones yielded high-amplitude radar reflection events. Notably, the clary-rich Tertiary limestones exhibit chaotic poor amplitude responses due to attenuation of radar waves (e.g., site 1: Fig. 9). The surficial occurrence of the KMF is not continuous and is largely blanketed by a thin cover of Quaternary sediments. The r1b-hso and r2-lpw representing Holocene and Late Pleistocene deposits respectively are stratified and possibly are reflections from fluvially reworked miliolite deposits. They are faulted internally, as indicated by subsidiary normal and reverse slip planes. Wedge/pinching out structures are interpreted as forming coarse-grained colluvial wedges (e.g., site 2: Fig. 10). The unconformable contact of Mesozoic/Tertiary and overlying Quaternary sediments is also well-imaged in all the radargrams. Between Lakhpat anticline and Ghuneri dome, the KMF, at places is buried under the thin cover of miliolite deposits (e.g., Fig. 4d and e).

Faults can be readily detected in radargrams if *(i)* different lithologies with/without varying amounts of clay content are juxtaposed across the fault, creating distinct radar facies between the hangingwall and footwall. The radar responses of varying lithologies can differ in terms of their amplitude, pattern, continuity and thickness. *(ii)* Continuous reflections are disrupted and displaced significantly along steeply dipping discontinuities. *(iii)* Faults juxtapose strata with varying dips, which generate significant changes in the geometry of the reflections (Ercoli et al., 2013). In the present study, most of the reflections are sub-horizontal away from the fault, but they indicate offset, change in dip or disruption if encountered by the fault. Warping or dragging of reflections is also noted. *(iv)* While at the edges of fault blocks or the subsurface presence of large boulders, diffraction hyperbolae form, none

of the radargrams shown in the present study attest to their existence (Grützner et al., 2012). Due to near-vertical dip, it was not possible to directly image the KMF in the radargram. In such case, the aforementioned key signatures were found useful to delineate the KMF.

The radargrams confirmed sub-seismic secondary fault strands distributed in the KMF zone. Slip definitely occurs along blind secondary strands and fault offsets in younger Quaternary sediments inferred from radargrams are the accurate measures of the recent seismicity in the study area. Though care was taken not to misinterpret the radargrams and to avoid mislabeling artifacts with prominent radar signatures as secondary slip planes. At site 1, the KMF does not displace Late Pleistocene colluvial wedge-outs (r2-lpw) (Fig. 9). The KMF with normal slip displaces Holocene (r1a-hso and r1b-hso) deposits at site 2 (Fig. 10). The KMF truncates Late Pleistocene channel-fill deposits (r2-lpw), which is located in the footwall. The normal and reverse slip planes offset colluvial wedge deposits (r2-lpw) at site 3 (Fig. 11). The Holocene deposits (r1b-hso) at site 4 are affected by planar and listric reverse slip planes (Fig. 12). Normal and reverse slip planes also affected the Holocene (r1a-hso) and colluvial wedge (r2-lpw) deposits at site 5 (Fig. 13). Pavan Kumar et al. (2018) also noted the presence of the synthetic and antithetic slip planes and interpreted them as forming a hybrid flower structure.

The structural interpretation of radargrams suggest that *(i)* the KMF (at sites 2, 3 and 4), and *(ii)* several of the secondary strands (e.g., at site 3: Fig. 11) offset or disrupt Quaternary deposits and therefore, they can be categorized as neotectonically active. Since the seismicity is majorly recorded from the eastern part of the KRB, the subsurface evidence presented in this paper, point that the western part of the KMF should not be neglected despite being showing low levels of seismicity. The fault zone stratigraphy inferred from radargrams is dissimilar with the dominantly rugged rocky terrain of the NHRFZ with insignificant Quaternary sediment cover.

7.1. Radar signatures of colluvial wedges and their neotectonic significance

The concealed earthquake-related structures, e.g., colluvial wedges, off-fault folding, secondary slip planes, seismites should be imaged by geophysical techniques to evaluate the neotectonic activity along the fault (Maurya et al., 1998; Pavan Kumar et al., 2018). A colluvial wedge is a wedge-shaped deposit that accumulates after a surface rupturing event at the base of a fault-scarp, and is the distinctive geological signature of an ancient dip-slip earthquake (McCalpin, 2009). Detecting wedges can be helpful in assessing the earthquake hazard of a region. Colluvial wedges have been imaged with the help of a range of geophysical techniques: *(i)* Electrical resistivity tomography (ERT) (McCalpin, 2009). Vanneste et al. (2006) identified three colluvial wedges in the hangingwall and deciphered at least three surface-rupturing paleo-earthquakes in southern Bulgaria. *(ii)* Seismic traveltime and waveform tomography techniques (Wasatch Fault, Utah: Buddensiek et al., 2008). P-wave seismic refraction tomography performed by Sheley et al. (2003) and other authors identified the colluvial wedges as low-velocity zones. However, the largest wedge could not be identified in the tomograms, and there were many small low-velocity zones in the tomogram that did not correspond to any colluvial wedge. *(iii)* McCalpin (2009) states that massive, moist saline soils are opaque to GPR response. However, prehistoric colluvial wedges formed of gravelly sand can be easily detected. In such a scenario, the GPR technique is effective to map the subsurface occurrence of the colluvial wedge in the KMF zone. This technique can be used extensively in other depositional environments. Christie et al. (2009), Carpentier et al. (2012a), (2012b), Ercoli et al. (2014), (2015) also interpreted colluvial wedges using GPR data.

In the present study, the scarp-derived colluvial wedge network and their internal structures are presented in the radargrams. The wedges consist of coarse-grained poorly-sorted blocky clasts of Bhuj sandstone
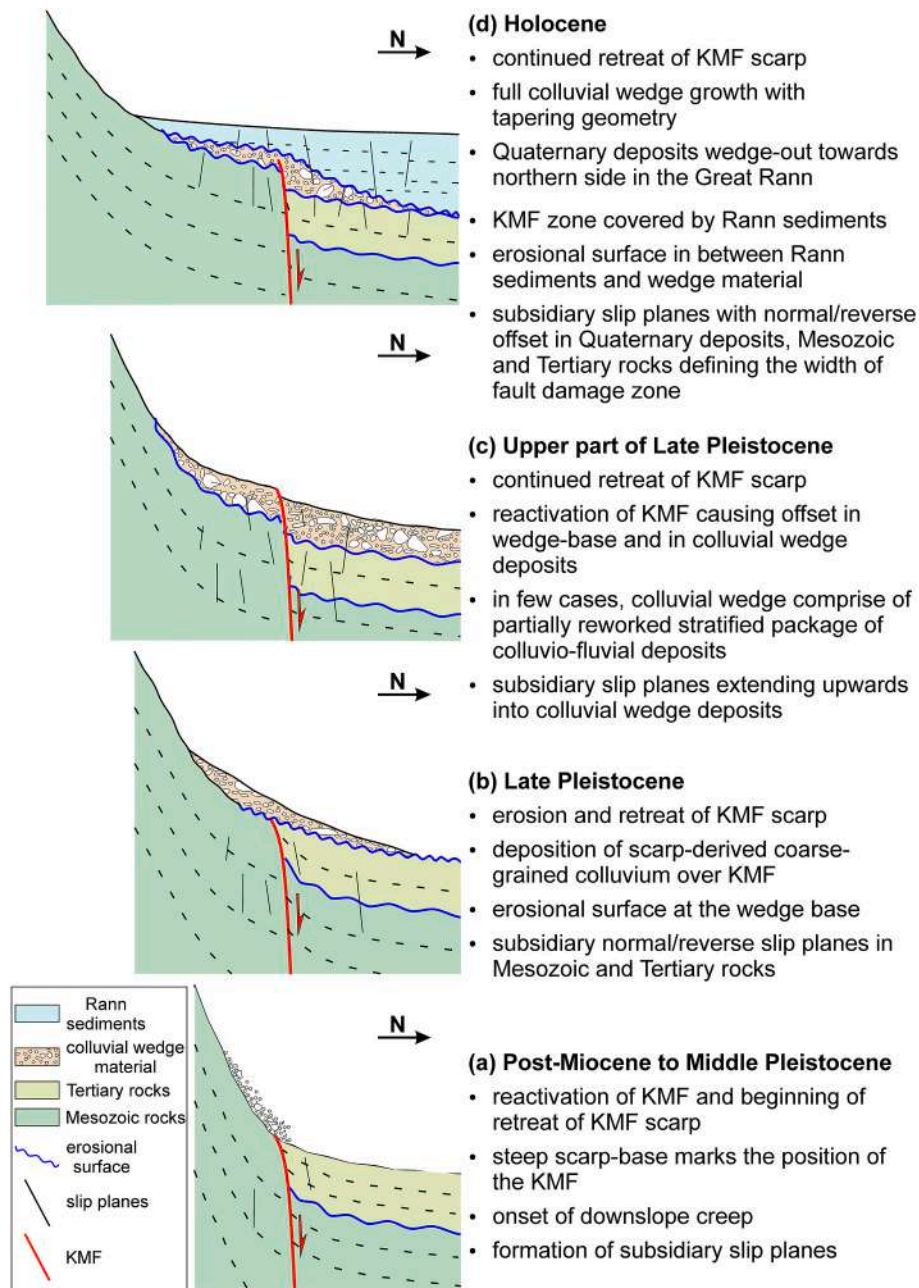
(d) Holocene
- continued retreat of KMF scarp
- full colluvial wedge growth with tapering geometry
- Quaternary deposits wedge-out towards northern side in the Great Rann
- KMF zone covered by Rann sediments
- erosional surface in between Rann sediments and wedge material
- subsidiary slip planes with normal/reverse offset in Quaternary deposits, Mesozoic and Tertiary rocks defining the width of fault damage zone

(c) Upper part of Late Pleistocene
- continued retreat of KMF scarp
- reactivation of KMF causing offset in wedge-base and in colluvial wedge deposits
- in few cases, colluvial wedge comprise of partially reworked stratified package of colluvio-fluvial deposits
- subsidiary slip planes extending upwards into colluvial wedge deposits

(b) Late Pleistocene
- erosion and retreat of KMF scarp
- deposition of scarp-derived coarse-grained colluvium over KMF
- erosional surface at the wedge base
- subsidiary normal/reverse slip planes in Mesozoic and Tertiary rocks

Legend:
- Rann sediments
- colluvial wedge material
- Tertiary rocks
- Mesozoic rocks
- erosional surface
- slip planes
- KMF

(a) Post-Miocene to Middle Pleistocene
- reactivation of KMF and beginning of retreat of KMF scarp
- steep scarp-base marks the position of the KMF
- onset of downslope creep
- formation of subsidiary slip planes

Fig. 14. Schematic cross-sections (not to scale) showing major stages of tectonic evolution of the Kachchh Mainland Fault (KMF) zone since Post-Miocene. Thickness of colluvial wedge is highly exaggerated.

and Tertiary limestones. The material that gathers at the base of steep mountain slopes is colluvium (Christie et al., 2009). As a result of scarp weathering and retreat, and redeposition of footwall detritus at the scarp toe over time, colluvial wedges form at the scarp-base (Christie et al., 2009). The colluvial wedges are represented in the radargrams by low to moderate amplitude zone and in the envelope attribute also, the low energy zone is identified easily. This resembles the findings of Sheley et al. (2003), who correlated the low-velocity regions in 2D refraction tomograms to the colluvial wedge.

The detection of wedge-shaped colluvial geometry in the landscape undergoing long-term rejuvenation demands significant effort. The tapered colluvial wedges are wrapped by the scarp-derived wash-off sediments, which are characterized by thick, long, continuous, parallel reflections suggesting well-stratified Late Pleistocene deposits, reflecting a period of seismic quiescence. Note that none of the radargrams

presented in this work record multiple colluvial wedges. All the wedges documented are in contact with the KMF and overlie it and a few of them are also affected and displaced by KMF. The colluvial wedges at sites 1 and 2 reflect low amplitude chaotic radar waves, whereas sites 3 and 5 show high amplitude semi-continuous to continuous reflections. At site 2, the colluvial wedge is translocated to the footwall (to the south) (Fig. 10). All the wedges thicken towards the main strand of KMF. The existence of colluvial wedges confirms the geophysical evidence for earthquake-related faulting. The on-fault scarp-derived colluvial wedges represent the post-seismic delayed response of the tectonic deformation along the KMF. The formation of colluvial wedges in all the cases in the vicinity of structural domes may represent a single faulting event. In site 3 radargram, folding of beds of Late Pleistocene deposits representing colluvial wedges above the KMF can be observed. The thickness of colluvial wedges varies in the KMF zone, with the thickest colluvial

wedge (~2 m) being found at site 3. The thickness of wedges can be used to estimate the amount of fault displacement and magnitude of earthquake (McCalpin, 2009).

The Late Pleistocene wedge-out material (r2-lpw) in the radargram taken at site 2 may represent paleo-channel fill deposits (Fig. 10). It reflects the paleo-course of the present-day north-flowing arid river channel nearby. Later on, the channel may have been truncated by the neotectonic movement along the KMF, which altered the channel course. In this case, the KMF served as a barrier to channel-fills and colluvial wedge deposits. The above interpretation appears to be correct, as the radargram was recorded over the terrace surface of a nearby river channel. It, thus, rules out the possibility that r2-lpw may represent a local conductive layer generating a typical pattern in case of strong attenuation.

The wedge-out geometry inferred from the radargrams may be confused with the gentler limbs of the anticlinally-formed geometry. But this interpretation can be negated since thin colluvial wedges are expressed in the form of a chaotic reflection pattern. Therefore, the cone-shaped anticlinal geometry should not be confused with the colluvial wedges or tapering river-fill geometry or alluvial fan facies comprising mainly Holocene alluvial deposits. Their radar facies specifically show the existence of poorly consolidated deposits, which are brittle in nature. So, not being ductile, folding is not possible.

7.2. Conceptual model of colluvial wedge formation

The study area offers a prime example of colluvial wedge formation and development of brittle structures in the KMF zone. Fig. 14 depicts the sequence of schematic cross-sections showing the evolution of colluvial wedge and associated deformed Quaternary deposits in the Cenozoic times. In the KRB, Paleocene, post-Paleocene, post-Miocene and Early Quaternary are the major periods of tectonics (follow Biswas, 1993 for more information). Shaikh et al. (2019) demonstrated the role of long-term landscape evolution in response to uplift-induced structurally controlled erosion along the western part of the KMF.

During post-Miocene to Mid-Pleistocene, ~W-striking uplift-bounding faults, including the KMF, were reactivated (Fig. 14a). This is marked by the faulted contact between the Mesozoic rocks and Miocene sediments defining the patchy surface trace of the KMF (Biswas, 1993; Chowksey et al., 2011a, 2011b; Maurya et al., 2017a; Shaikh et al., 2019). This time interval represents a long period of non-deposition and erosion of the paleo-scarp owing to the hyper-arid climatic regime. The erosion, induced by fluvial and other geomorphic processes, of the softer lithologies exposed on the northern scarp-face resulted in further southward retreat and upliftment of the paleo-scarp. This led to the onset of downslope creep of the colluvial sediments. The generated material was subsequently transported northward and deposited on to the downthrown block. Thus, the steep north-dipping deformed Mesozoic rocks exposed at the scarp-face served as the provenance. The colluvial deposits are confined exclusively in the KMF zone, near the scarp-base. There is no scope of lateral extension of colluvial wedge further northward in the Great Rann. Only a few subsidiary normal and reverse slip planes were developed in the KMF zone.

The degradation and retreat of paleo-scarp continued during the Late Pleistocene. Periodic tectonic movement along the KMF triggered uplift of the NHRFZ that led to attain the present height of the scarp. The continuous deposition of coarse-grained colluvial sediments over the KMF formed a thin colluvial wedge cover (Fig. 14b). Though there is paucity of information of the presence of colluvial wedges in the fault zone, their formation in the seismically active terrain like KRB is obvious. The deposits may have been partially reworked as seen in the previously described analogous deposits exposed in the eastern part of the KMF zone (Chowksey et al., 2011b). The phase of deposition was followed by erosion leading to formation of erosional surface over the wedge. The Mesozoic and Tertiary rocks were again offset by subsidiary slip planes.

The offset of the earlier formed colluvial wedge took place due to continued reactivation of the KMF during the end phase of Late Pleistocene (Fig. 14c). The scarp produced was flattened through erosion. The continued scarp retreat and consequent redeposition of scarp-derived stratified partially reworked colluvio-fluvial sediments over the KMF took place (Figs. 11 and 13). The later scarp-derived material acted as a filling up over the colluvial wedges. The slip planes were increased in number, and they offset the wedge as well along with disrupting the Mesozoic and Tertiary rocks (e.g., Fig. 13).

During Holocene, the submergence of KMF zone by shallow sea took place which led to deposition of marine sediments of the Great Rann (Kumar et al., 2021). Marginal marine conditions prevailed until the last ~2000 years BP leaving a flat saline surface of the Great Rann abutting against the KMF scarp. This led to the generation of partially consolidated Holocene sediments forming a top layer in the KMF zone, responsible for retaining the wedge shape (Fig. 14d). Numerous slip planes were developed disturbing the Holocene sediments, Late Pleistocene colluvial wedge, Mesozoic and Tertiary rocks. The sub-seismic occurrence of slip planes now define the full width of the KMF zone.

8. Conclusions

The present work illustrates the importance of using GPR to constrain the geometry of subsurface structures and fault zone strata. High-resolution GPR data integrated with the surface geological observations along the western part of the KMF in the KRB has provided critical data for shallow subsurface fault mapping and fault geometry in contemporary seismotectonic setting. GPR surveys provided accurate radargrams of brittle deformation within the active KMF zone. This case study can work as a guide on how to locate the concealed fault zone in like depositional settings. The GPR signals penetrated at least 8 m depth using a 200 MHz frequency monostatic antenna with excellent resolution of the subsurface stratigraphy.

1. Shallow subsurface geophysical studies using ground-penetrating radar (GPR), carried out at the western Kachchh Mainland Fault (KMF) in the western part of the Kachchh rift basin (KRB) in general points to near-vertical north-dipping normal fault. The GPR studies along the western part of the KMF fits with the field geological observations. This work confirms that the KMF regionally is listric but may not have a simple curved geometry. The previous tectonic model considers the KMF to be a plunging upthrust. With such a complex geometry, more structural details need to be added to the existing tectonic model in the future.

2. Segmented nature of the western part of the KMF is supported by NW- to NE-striking oblique-slip transverse faults. It also points to crucial role of transverse faults responsible for the change in strike of the KMF and variation in seismicity along the KMF. These transverse faults may play a key role in stress transfer between uplift-bounding KMF and intra-uplift Vigodi-Gugriana-Khirasra-Netra Fault System (VGKNFS).

3. The approach of field observations combined with extensive GPR work was found to be useful in building neotectonic framework of the KMF. From the KRB, the present work is the maiden attempt at detecting the potential existence of sub-seismic colluvial wedges. Most colluvial wedges, like low-velocity seismic tomogram findings, are associated with the low amplitude EM wave zone with semi-continuous to chaotic reflections. On the other hand, stacked, high amplitude cone-shaped reflections of the potential colluvial wedge are also observed. The energy-based and phase attribute enhanced the structural interpretation of radargrams.

4. Multiple secondary synthetic and antithetic normal and reverse slip planes were detected in radargrams. None of the slip planes were having surficial occurrence due to continuous sedimentation record towards the downthrown block of the KMF. These secondary slip planes may be the branch faults splaying from the primary KMF at

depth. Upon reaching up the surface, they displace and warp etc. the Quaternary sediments suggesting neotectonic deformation. The evidence of drainage deflection/termination along the KMF is reported. Based on the GPR studies, the imaged brittle deformation evidence accompanied by the presence of potential colluvial wedges, it is inferred that the western part of the KMF is neotectonically active.

5. A schematic model for the development of colluvial wedges and related deformed Quaternary deposits in the Cenozoic is presented. Since post-Miocene times, continued erosion of the paleo-scarp resulted in the downslope creep and subsequent deposition of the colluvial sediments on to the downthrown block, which formed a colluvial wedge. The continued reactivation of the KMF during the end phase of Late Pleistocene offset of the earlier formed colluvial wedge.

6. The colluvial wedge, an indicator of neotectonically active nature of the KMF, achieved its maximum growth with tapering geometry during Holocene. The deposition of marginal marine sediments in the downthrown block formed a top layer in the KMF zone, which concealed the colluvial wedge and KMF.

CRediT authorship contribution statement

Mohamedharoon A. Shaikh: Conceptualization, Methodology, Software, Formal analysis, Investigation, Data collection and Interpretation, Writing – original draft, Writing – review & editing, Visualization. **Atul K. Patidar:** Methodology, Interpretation, Validation, Writing – review & editing, Visualization. **Deepak M. Maurya:** Conceptualization, Methodology, Investigation, Validation, Resources, Supervision, Writing – original draft, Writing – review & editing, Project administration. **Naimisha P. Vanik:** Investigation. **Akash Padmalal:** Investigation. **Prabhuti Tiwari:** Investigation. **Soumyajit Mukherjee:** Writing – review & editing. **Laxman S. Chamyal:** Investigation, Supervision, Validation, Writing – review & editing, Project administration.

Declaration of competing interest

The authors declare that they have no known competing financial interests or personal relationships that could have appeared to influence the work reported in this paper.

Acknowledgements

Appendix A. Supplementary data

Supplementary data to this article can be found online at https://doi. org/10.1016/j.jsg.2022.104526.

References

Azeez, K.A., Mohan, K., Veeraswamy, K., Rastogi, B.K., Gupta, A.K., Harinarayana, T., 2018. 3D crustal resistivity structure beneath the Wagad aftershock zone of the 2001 Bhuj earthquake, Kutch, India: heterogeneous resistivity structure controlled by widespread fluid infiltration and clues to aftershocks pattern. Tectonophysics 747, 54–67. https://doi.org/10.1016/j.tecto.2018.09.014.

Azeez, K.K., Mohan, K., Veeraswamy, K., Rastogi, B.K., Gupta, A.K., Harinarayana, T., 2021. Lithospheric resistivity structure of the 2001 Bhuj earthquake aftershock zone. Geophys. J. Int. 224, 1980–2000. https://doi.org/10.1093/gji/ggaa556.

Bendick, R., Bilham, R., Fielding, E., Gaur, V.K., Hough, S.E., Kier, G., Kulkarni, M.N., Martin, S., Mueller, K., Mukul, M., 2001. The 26 January 2001 "Republic Day"

earthquake, India. Seismol Res. Lett. 72, 328–335. https://doi.org/10.1785/gssrl.72.3.328.

Beres, M., Huggenberger, P., Green, A.G., Horstmeyer, H., 1999. Using two-and three-dimensional georadar methods to characterize glaciofluvial architecture. Sediment. Geol. 129, 1–24. https://doi.org/10.1016/S0037-0738(99)00053-6.

Berton, F., Guedes, C.C.F., Vesely, F.F., Souza, M.C., Angulo, R.J., Rosa, M.L.C.C., Barboza, E.G., 2019. Quaternary coastal plains as reservoir analogs: wave-dominated sand-body heterogeneity from outcrop and ground-penetrating radar, central Santos Basin, southeast Brazil. Sediment. Geol. 379, 97–113. https://doi.org/10.1016/j.sedgeo.2018.11.008.

Bilham, R., 1999. Slip Parameters for the Rann of Kachchh, India, 16 June 1819, Earthquake, Quantified from Contemporary Accounts, 146. Geological Society, London, Special Publications, pp. 295–319. https://doi.org/10.1144/GSL.SP.1999.146.01.18.

BIS, 2002. IS 1893–2002 (Part 1): Indian Standard Criteria for Earthquake Resistant Design of Structures, Part 1–General Provisions and Buildings. Bureau of Indian Standards, New Delhi. Retrieved from. https://bis.gov.in/other/quake.htm.

Biswas, S.K., 1993. Geology of Kutch. K. D. Malaviya Institute of Petroleum Exploration, Dehradun.

Biswas, S.K., 2016. Tectonic framework, structure and tectonic evolution of Kutch Basin, western India. Geol. Soc. India 6, 129–150. https://doi.org/10.17491/cgsi/2016/105417.

Brozzetti, F., Cirillo, D., de Nardis, R., Cardinali, M., Lavecchia, G., Orecchio, B., Presti, D., Totaro, C., 2017. Newly identified active faults in the Pollino seismic gap, southern Italy, and their seismotectonic significance. J. Struct. Geol. 94, 13–31. https://doi.org/10.1016/j.jsg.2016.10.005.

Buddensiek, M.L., Sheng, J., Crosby, T., Schuster, G.T., Bruhn, R.L., He, R., 2008. Colluvial wedge imaging using traveltime and waveform tomography along the Wasatch Fault near Mapleton, Utah. Geophys. J. Int. 172, 686–697. https://doi.org/10.1111/j.1365-246X.2007.03667.x.

Carpentier, S.F.A., Green, A.G., Doetsch, J., Dorn, C., Kaiser, A.E., Campbell, F., Horstmeyer, H., Finnemore, M., 2012a. Recent deformation of Quaternary sediments as inferred from GPR images and shallow P-wave velocity tomograms: northwest Canterbury Plains, New Zealand. J. Appl. Geophys. 81, 2–15. https://doi.org/10.1016/j.jappgeo.2011.09.007.

Carpentier, S.F.A., Green, A.G., Langridge, R., Boschetti, S., Doetsch, J., Abächerli, A.N., Horstmeyer, H., Finnemore, M., 2012b. Flower structures and Riedel shears at a step over zone along the Alpine Fault (New Zealand) inferred from 2-D and 3-D GPR images. J. Geophys. Res. Solid Earth 117 (B2). https://doi.org/10.1029/2011JB008749.

Cassidy, N.J., 2009. Ground penetrating radar data processing, modelling and analysis. In: Jol, H.M. (Ed.), Ground Penetrating Radar Theory and Applications. Elsevier, New York, pp. 141–176.

Chandra, U., 1977. Earthquakes of peninsular India—a seismotectonic study. Bull. Seismol. Soc. Am. 67, 1387–1413. https://doi.org/10.1785/BSSA0670051387.

Chandrasekhar, D.V., Mishra, D.C., 2002. Some geodynamic aspects of Kachchh basin and seismicity: an insight from gravity studies. Curr. Sci. 83, 492–498.

Chandrasekhar, E., Mathew, G., Harinarayana, T., 2012. A new hypothesis for the deep subsurface structures near the Bhuj 2001 earthquake (M w 7.6) hypocentre zone and its tectonic implications. Geophys. J. Int. 190, 761–768. https://doi.org/10.1111/j.1365-246X.2012.05532.x.

Chaudhary, P., Mohan, K., Chaudhary, B.S., 2019. Magnetotellurics study to identify subsurface resistivity structure in the eastern part of Kachchh (Little rann area) of Gujarat, India. Pure Appl. Geophys. 176, 2479–2496. https://doi.org/10.1007/s00024-019-02102-w.

Choudhury, P., Chopra, S., Kumar, M.R., 2018. A review of seismic hazard assessment of Gujarat: a highly active intra-plate region. Earth Sci. Rev. 187, 205–218. https://doi.org/10.1016/j.earscirev.2018.09.014.

Chowksey, V., Joshi, P., Maurya, D.M., Chamyal, L.S., 2011a. Ground penetrating radar characterization of fault-generated Quaternary colluvio-fluvial deposits along the seismically active Kachchh Mainland Fault, Western India. Curr. Sci. 100, 915–921. https://www.jstor.org/stable/24076485.

Chowksey, V., Maurya, D.M., Joshi, P., Khonde, N., Das, A., Chamyal, L.S., 2011b. Lithostratigraphic development and neotectonic significance of the Quaternary sediments along the Kachchh Mainland Fault (KMF) zone, western India. J. Earth Syst. Sci. 120, 979–999. https://doi.org/10.1007/s12040-011-0123-0.

Chowksey, V., Maurya, D.M., Khonde, N., Chamyal, L.S., 2010. Tectonic geomorphology and evidence for active tilting of the Bela, Khadir and Bhanjada islands in the seismically active Kachchh palaeorift graben, Western India. Z. Geomorphol. 54, 467–490. https://doi.org/10.1127/0372-8854/2010/0054-0021.

Christie, M., Tsoflias, G.P., Stockli, D.F., Black, R., 2009. Assessing fault displacement and off-fault deformation in an extensional tectonic setting using 3-D ground-penetrating radar imaging. J. Appl. Geophys. 68, 9–16. https://doi.org/10.1016/j.jappgeo.2008.10.013.

Chung, W.Y., Gao, H., 1995. Source parameters of the Anjar earthquake of July 21, 1956, India, and its seismotectonic implications for the Kutch rift basin. Tectonophysics 242, 281–292. https://doi.org/10.1016/0040-1951(94)00203-L.

Cinti, F.R., Pauselli, C., Livio, F., Ercoli, M., Brunori, C.A., Ferrario, M.F., Volpe, R., Civico, R., Pantosti, D., Pinzi, S., De Martini, P.M., Ventura, G., Alfonsi, L., Gambillara, R., Michetti, A.M., 2015. Integrating multidisciplinary, multiscale geological and geophysical data to image the Castrovillari fault (Northern Calabria, Italy). Geophys. J. Int. 203, 1847–1863. https://doi.org/10.1093/gji/ggv404.

Dasgupta, T., Mukherjee, S., 2020. Sediment Compaction and Applications in Petroleum Geoscience. Springer, Series. Advances in Oil and Gas Exploration & Production. ISSN: 2509-372X.

Dasgupta, S., Pande, P., Iqbal, Z., Sanyal, N.V., et al., 2000. Seismotectonic Atlas of India and its Environs. Geological Survey of India.

Davis, J.L., Annan, A.P., 1989. Ground-penetrating radar for high resolution mapping of soil and rock stratigraphy. Geophys. Prospect. 37, 531–551. https://doi.org/10.1111/j.1365-2478.1989.tb02221.x.

Ékes, C., Friele, P., 2003. Sedimentary Architecture and Post-glacial Evolution of Cheekye Fan, Southwestern British Columbia, Canada, 211. Geological Society, London, Special Publications, pp. 87–98. https://doi.org/10.1144/GSL.SP.2001.211.01.08.

Ercoli, M., Cirillo, D., Pauselli, C., Jol, H.M., Brozzetti, F., 2021. GPR signature of Quaternary faulting: a study from the Mt. Pollino region, southern Apennines, Italy. Solid Earth Discuss. 1–35. https://doi.org/10.5194/se-2021-75.

Ercoli, M., Pauselli, C., Francesca, R.C., Emanuele, F., Roberto, V., 2015. Imaging of an active fault: comparison between 3D GPR data and outcrops at the Castrovillari fault. Interpretation 3, SY57–SY66. https://doi.org/10.1190/INT-2014-0234.1. Calabria, Italy.

Ercoli, M., Pauselli, C., Frigeri, A., Forte, E., Federico, C., 2013. "Geophysical paleoseismology" through high resolution GPR data: a case of shallow faulting imaging in Central Italy. J. Appl. Geophys. 90, 27–40. https://doi.org/10.1016/j.jappgeo.2012.12.001.

Ercoli, M., Pauselli, C., Frigeri, A., Forte, E., Federico, C., 2014. 3-D GPR data analysis for high-resolution imaging of shallow subsurface faults: the Mt Vettore case study (Central Apennines, Italy). Geophys. J. Int. 198, 609–621. https://doi.org/10.1093/gji/ggu156.

Falcucci, E., Gori, S., Moro, M., Fubelli, G., Saroli, M., Chiarabba, C., Galadini, F., 2015. Deep reaching versus vertically restricted Quaternary normal faults: implications on seismic potential assessment in tectonically active regions: lessons from the middle Aterno valley fault system, central Italy. Tectonophysics 651, 186–198. https://doi.org/10.1016/j.tecto.2015.03.021.

Green, A., Gross, R., Holliger, K., Horstmeyer, H., Baldwin, J., 2003. Results of 3-D georadar surveying and trenching the San Andreas fault near its northern landward limit. Tectonophysics 368, 7–23. https://doi.org/10.1016/S0040-1951(03)00147-1.

Grützner, C., Reicherter, K., Hübscher, C., Silva, P.G., 2012. Active faulting and neotectonics in the Baelo Claudia area, Campo de Gibraltar (southern Spain). Tectonophysics 554, 127–142. https://doi.org/10.1016/j.tecto.2012.05.025.

Guha, A., Chattoraj, S.L., Chatterjee, S., Kumar, K.V., Rao, P.V.N., Bhaumik, A.K., 2020. Reflectance Spectroscopy-Guided Broadband Spectral Derivative Approach to Detect Glauconite-Rich Zones in Fossiliferous Limestone, Kachchh Region, Gujarat, India. Ore Geology Reviews, p. 103825. https://doi.org/10.1016/j.oregeorev.2020.103825.

Jiang, X., Li, Z., Li, C., Gong, W., 2019. A gravity study of the Longmenshan Fault Zone: new insights into the nature and evolution of the fault zone and extrusion-style growth of the Tibetan Plateau since 40 Ma. Tectonics 38, 176–189. https://doi.org/10.1029/2018TC005272.

Jol, H.M., 2009. Ground Penetrating Radar: Theory and Applications, first ed. Elsevier, Amsterdam. https://doi.org/10.1016/B978-0-444-53348-7.X0001-4.

Jol, H.M., Bristow, C.S., 2003. GPR in Sediments: Advice on Data Collection, Basic Processing and Interpretation, a Good Practice Guide, 211. Special publication-Geological Society of London, pp. 9–28. https://doi.org/10.1144/GSL.SP.2001.211.01.02.

Joshi, P., Maurya, D.M., Chowksey, V., Chamyal, L.S., 2012. Shallow subsurface mapping of active faults using GPR in the seismically active Kachchh palaeo-rift basin, Western India: implication for neotectonic activity. In: 14th International Conference on Ground Penetrating Radar (GPR), pp. 844–849. https://doi.org/10.1109/ICGPR.2012.6254980. Shanghai, China, 2012.

Khonde, N., Maurya, D.M., Singh, A.D., Chowksey, V., Chamyal, L.S., 2011. Environmental significance of raised rann sediments along the margins of Khadir, Bhanjada and Kuar Bet islands in Great rann of Kachchh, western India. Curr. Sci. 101, 1429–1434. https://www.jstor.org/stable/24080220.

Kumar, A., Maurya, D.M., Khonde, N., Phartiyar, B., Arif, M., Giosan, L., Chamyal, L.S., 2021. Holocene paleoenvironmental changes in the marginal marine basin of Great Rann of Kachchh, western India: insights from sedimentological and mineral magnetic studies on a ~60 m long core. Quat. Int.

Lacan, P., Nivière, B., Rousset, D., Sénéchal, P., 2012. Late Pleistocene folding above the Mail Arrouy Thrust, north-western Pyrenees (France). Tectonophysics 541, 57–68. https://doi.org/10.1016/j.tecto.2012.03.022.

Li, K., Xu, X., Kirby, E., Tang, F., Kang, W., 2018. Late quaternary paleoseismology of the Milin fault: implications for active tectonics along the Yarlung Zangbo Suture, Southeastern Tibet plateau. Tectonophysics 731, 64–72. https://doi.org/10.1016/j.tecto.2017.12.026.

Liberty, L.M., Hemphill-Haley, M.A., Madin, I.P., 2003. The Portland Hills Fault: uncovering a hidden fault in Portland, Oregon using high-resolution geophysical methods. Tectonophysics 368, 89–103. https://doi.org/10.1016/S0040-1951(03)00152-5.

Lunina, O.V., Denisenko, I.A., 2020. Single-event throws along the Delta Fault (Baikal Rift) reconstructed from ground penetrating radar, geological and geomorphological data. J. Struct. Geol. 141, 104209. https://doi.org/10.1016/j.jsg.2020.104209.

Lunina, O.V., Gladkov, A.S., Afonkin, A.M., Serebryakov, E.V., 2016. Deformation style in the damage zone of the Mondy fault: GPR evidence (Tunka basin, southern East Siberia). Russ. Geol. Geophys. 57, 1269–1282. https://doi.org/10.1016/j.rgg.2016.08.012.

Machuca, S., García-Delgado, H., Velandia, F., 2021. Studying active fault-related folding on tectonically inverted orogens: a case study at the Yariguíes Range in the Colombian Northern Andes. Geomorphology 375, 107515. https://doi.org/10.1016/j.geomorph.2020.107515.

Magalhães, A.J.C., Lima-Filho, F.P., Guadagnin, F., Silva, V.A., Teixeira, W.L.E., Souza, A.M., Raja Gabaglia, G.P., Catuneanu, O., 2017. Ground penetrating radar for facies architecture and high-resolution stratigraphy: examples from the Mesoproterozoic in the Chapada Diamantina Basin, Brazil. Mar. Petrol. Geol. 86, 1191–1206. https://doi.org/10.1016/j.marpetgeo.2017.07.027.

Maurya, D.M., Chowksey, V., Joshi, P.N., Chamyal, L.S., 2013. Application of GPR for delineating the neotectonic setting and shallow subsurface nature of the seismically active Gedi fault, Kachchh, western India. J. Geophys. Eng. 10, 034006 https://doi.org/10.1088/1742-2132/10/3/034006.

Maurya, D.M., Chowksey, V., Patidar, A.K., Chamyal, L.S., 2017a. A review and new data on the neotectonic evolution of active faults in the Kachchh Basin, Western India: legacy of post-Deccan Trap tectonic inversion. In: Mukherjee, S., Misra, A.A., Calve's, G., Nemcok, M. (Eds.), Tectonics of Deccan Large Igneous Province, 445. Geological Society of London Special Publication, London, pp. 237–268. https://doi.org/10.1144/SP445.7.

Maurya, D.M., Chowksey, V., Tiwari, P., Chamyal, L.S., 2017b. Tectonic geomorphology and neotectonic setting of the seismically active South Wagad Fault (SWF), Western India, using field and GPR data. Acta Geophys. 65, 1167–1184. https://doi.org/10.1007/s11600-017-0099-5.

Maurya, D.M., Goyal, B., Patidar, A.K., Mulchandani, N., Thakkar, M.G., Chamyal, L.S., 2006. Ground Penetrating Radar imaging of two large sand blow craters related to the 2001 Bhuj earthquake, Kachchh, Western India. J. Appl. Geophys. 60, 142–152. https://doi.org/10.1016/j.jappgeo.2006.02.001.

Maurya, D.M., Rachna, R., Chamyal, L.S., 1998. Seismically induced deformational structures (seismites) from the Mid-Late Holocene terraces, lower Mahi valley, Gujarat. J. Geol. Soc. India 51, 755–758.

Maurya, D.M., Shaikh, M.A., Mukherjee, S., 2021a. Comment on "structural attributes and paleostress analysis of quaternary landforms along the Vigodi Fault (VF) in western Kachchh region. Quat. Int. 601, 143–147. https://doi.org/10.1016/j.quaint.2021.04.029. Quat. Int. 10.1016/j.quaint.2020.07.038]".

Maurya, D.M., Thakkar, M.G., Chamyal, L.S., 2003a. Implications of transverse fault system on tectonic evolution of Mainland Kachchh, western India. Curr. Sci. 85, 661–667. https://www.jstor.org/stable/24109108.

Maurya, D.M., Thakkar, M.G., Chamyal, L.S., 2003b. Quaternary geology of the arid zone of Kachchh: terra incognita. Proc. Indian Nat. Sci. Acad. 69, 123–136.

Maurya, D.M., Thakkar, M.G., Khonde, N., Chamyal, L.S., 2009. Geomorphology of the little rann of Kachchh, W. India: implication for basin architecture and Holocene palaeo-oceanographic conditions. Z. Geomorphol. 53, 69–80. https://doi.org/10.1127/0372-8854/2009/0053-0069.

Maurya, D.M., Tiwari, P., Shaikh, M.A., Patidar, A.K., Vanik, N., Padmalal, A., Chamyal, L.S., 2021b. Late Quaternary drainage reorganization assisted by surface faulting: the example of the Katrol Hill Fault zone, Kachchh, Western India. Earth Surf. Process. Landforms 46, 1268–1293. https://doi.org/10.1002/esp.5097.

McCalpin, J.P., 2009. Paleoseismology, second ed. Academic press, Cambridge.

McClymont, A.F., Green, A.G., Streich, R., Horstmeyer, H., Tronicke, J., Nobes, D.C., Pettinga, J., Campbell, J., Langridge, R., 2008a. Visualization of active faults using geometric attributes of 3D GPR data: an example from the Alpine Fault Zone, New Zealand. Geophysics 73, B11–B23. https://doi.org/10.1190/1.2825408.

McClymont, A.F., Green, A.G., Villamor, P., Horstmeyer, H., Grass, C., Nobes, D.C., 2008b. Characterization of the shallow structures of active fault zones using 3-D ground-penetrating radar data. J. Geophys. Res. Solid Earth 113, B10315. https://doi.org/10.1029/2007JB005402.

McClymont, A.F., Villamor, P., Green, A.G., 2009. Fault displacement accumulation and slip rate variability within the Taupo Rift (New Zealand) based on trench and 3-D ground-penetrating radar data. Tectonics 28, TC4005. https://doi.org/10.1029/2008TC002334.

McClymont, A.F., Green, A.G., Kaiser, A., Horstmeyer, H., Langridge, R., 2010. Shallow fault segmentation of the Alpine fault zone, New Zealand revealed from 2-and 3-D GPR surveying. J. Appl. Geophys. 70, 343–354. https://doi.org/10.1016/j.jappgeo.2009.08.003.

Mishra, D.C., Chandrasekhar, D.V., Singh, B., 2005. Tectonics and crustal structures related to Bhuj earthquake of January 26, 2001: based on gravity and magnetic surveys constrained from seismic and seismological studies. Tectonophysics 396, 195–207. https://doi.org/10.1016/j.tecto.2004.12.007.

Mohan, D., Chaudhary, P., Patel, P., Chaudhary, B.S., Chopra, S., 2018. Magnetotelluric study to characterize Kachchh Mainland Fault (KMF) and Katrol Hill Fault (KHF) in the western part of Kachchh region of Gujarat, India. Tectonophysics 726, 43–61. https://doi.org/10.1016/j.tecto.2018.01.018.

Mohan, K., Rastogi, B.K., Chaudhary, P., 2015. Magnetotelluric studies in the epicenter zone of 2001, Bhuj earthquake. J. Asian Earth Sci. 98, 75–84. https://doi.org/10.1016/j.jseaes.2014.10.019.

Mukherjee, S., 2014. Review of flanking structures in meso- and micro-scales. Geological Magazine 151 (6), 957–974. https://doi.org/10.1017/S0016756813001088.

Naganjaneyulu, K., Ledo, J.J., Queralt, P., 2010. Deep crustal electromagnetic structure of Bhuj earthquake region (India) and its implications. Geol. Acta 18, 83–97. https://doi.org/10.1344/105.000001517.

Nagar, M., Kumar, G.P., Mahesh, P., Rakesh, N., Chouhan, A.K., Nagarujna, D., Chopra, S., Kumar, M.R., 2021. Magnetotelluric evidence for trapped fluids beneath the seismogenic zone of the Mw6. 0 Anjar earthquake, Kachchh intraplate region, northwest India. Tectonophysics 814, 228969. https://doi.org/10.1016/j.tecto.2021.228969.

Nobes, D.C., Hornblow, S.M., 2021. Not all faults are conductive: the effects of seasonal weather changes on the near-surface expression of faults. Geophys. Prospect. 69, 1503–1514. https://doi.org/10.1111/1365-2478.13126.

Okada, T., Iio, Y., Matsumoto, S., Bannister, S., Ohmi, S., Horiuchi, S., Sato, T., Miura, T., Pettinga, J., Ghisetti, F., Sibson, R.H., 2019. Comparative tomography of reverse-slip and strike-slip seismotectonic provinces in the northern South Island, New Zealand. Tectonophysics 765, 172–186. https://doi.org/10.1016/j.tecto.2019.03.016.

Padmalal, A., Khonde, N., Maurya, D.M., Shaikh, M., Kumar, A., Vanik, N., Chamyal, L. S., 2019. Geomorphic characteristics and morphologic dating of the Allah Bund fault scarp, Great rann of Kachchh, western India. In: Mukherjee, S. (Ed.), Tectonics and Structural Geology: Indian Context. Springer, Berlin, pp. 55–74. https://doi.org/10.1007/978-3-319-99341-6_3.

Padmalal, A., Maurya, D.M., Vanik, N.P., Shaikh, M.A., Tiwari, P., Chamyal, L.S., 2021. Impact of long term uplift on stream networks in tectonically active Northern Hill Range, Kachchh palaeo-rift basin, western India. J. Mt. Sci. 18, 1609–1629. https://doi.org/10.1007/s11629-020-6420-9.

Pandey, D., Lucy, M., Martin, S., Satish, S., 2008a. Feasibility of using the magnetotelluric method for sub-basalt imaging at Kachchh, India. Appl. Geophys. 5, 74–82. https://doi.org/10.1007/s11770-008-0008-4.

Pandey, D., Sinha, M., MacGregor, L., Singh, S., 2008b. Ocean coast effect on magnetotelluric data: a case study from Kachchh, India. Mar. Geophys. Res. 29, 185–193. https://doi.org/10.1007/s11001-008-9057-6.

Pandey, D., Singh, S., Sinha, M., MacGregor, L., 2009. Structural imaging of Mesozoic sediments of Kachchh, India, and their hydrocarbon prospects. Mar. Petrol. Geol. 26, 1043–1050. https://doi.org/10.1016/j.marpetgeo.2008.07.005.

Pandey, D., Pandey, A., Rajan, S., 2010. Mode-Converted (P-SV) waves for imaging thin intercalated Basaltic layers and their possible geologic implications. Nat. Resour. Res. 19, 141–150. https://doi.org/10.1007/s11053-010-9116-y.

Pandey, D.K., Pandey, A., Rajan, S., 2011. Offshore extension of Deccan Traps in Kachchh, central western India: implications for geological sequestration studies. Nat. Resour. Res. 20, 33–43. https://doi.org/10.1007/s11053-010-9133-x.

Patel, P., Mohan, K., Chaudhary, P., 2020. Estimation of sediment thickness (including Mesozoic) in the western central part of Kachchh Basin, Gujarat (India) using Magnetotellurics. J. Appl. Geophys. 173, 103943. https://doi.org/10.1016/j.jappgeo.2020.103943.

Patidar, A.K., Maurya, D.M., Thakkar, M.G., Chamyal, L.S., 2007. Fluvial geomorphology and neotectonic activity based on field and GPR data, Katrol hill range, Kachchh, western India. Quat. Int. 159, 74–92. https://doi.org/10.1016/j.quaint.2006.08.013.

Patidar, A.K., Maurya, D.M., Thakkar, M.G., Chamyal, L.S., 2008. Evidence of neotectonic reactivation of the Katrol Hill Fault during late quaternary and its GPR characterization. Curr. Sci. 94, 338–346. https://www.jstor.org/stable/24100341.

Pavan Kumar, G., Chaudhary, I., Nagar, M., Chouhan, A., Prizomwala, S.P., Mahesh, P., Chopra, S., 2018. Transient Electromagnetic investigations in a tectonic domain of the Kachchh intraplate region, western India: a morphotectonic study of the Kachchh Mainland Fault. Tectonics 37, 4239–4260. https://doi.org/10.1002/2017GL072936.

Pavan Kumar, G., Mahesh, P., Nagar, M., Mahender, E., Kumar, V., Mohan, K., Ravi Kumar, M., 2017a. Role of deep crustal fluids in the genesis of intraplate earthquakes in the Kachchh region, northwestern India. Geophys. Res. Lett. 44, 4054–4063. https://doi.org/10.1002/2017GL072936.

Pavan Kumar, G., Kumar, V., Nagar, M., Singh, D., Mahendar, E., Patel, P., Mahesh, P., 2017b. Magnetotelluric impedance tensor analysis for identification of transverse tectonic feature in the Wagad uplift, Kachchh, northwest India. J. Earth Syst. Sci. 126, 1–13. https://doi.org/10.1007/s12040-017-0851-x.

Pavan Kumar, G., Nagar, M., Choudhary, V., Prasad, A.D., 2019. Shallow subsurface imaging of the Wagad active fault system (Kachchh, northwestern India) by time domain electromagnetic studies. J. Earth Syst. Sci. 128, 1–14. https://doi.org/10.1007/s12040-019-1090-0.

Pousse-Beltran, L., Vassallo, R., Audemard, F., Jouanne, F., Oropeza, J., Garambois, S., Aray, J., 2018. Earthquake geology of the last millennium along the Boconó Fault, Venezuela. Tectonophysics 747, 40–53. https://doi.org/10.1016/j.tecto.2018.09.010.

Prasad, B.R., Venkateswarlu, N., Prasad, A., Murthy, A., Sateesh, T., 2010. Basement configuration of on-land Kutch basin from seismic refraction studies and modeling of first arrival travel time skips. J. Asian Earth Sci. 39, 460–469. https://doi.org/10.1016/j.jseaes.2010.04.003.

Rajendran, K., Rajendran, C.P., Thakkar, M., Tuttle, M.P., 2001. The 2001 Kutch (Bhuj) earthquake: coseismic surface features and their significance. Curr. Sci. 80, 1397–1405. https://www.jstor.org/stable/24104957.

Rao, P.S., Arora, B.R., Singh, A.K., 2014. Electrical conductance map for the Kachchh rift basin: constraint on tectonic evolution and seismotectonic implications. Pure Appl. Geophys. 171, 2353–2370. https://doi.org/10.1007/s00024-014-0846-3.

Rastogi, B.K., Gupta, H.K., Mandal, P., Satyanarayana, H.V.S., Kousalya, M., Raghavan, R., Jain, R., Sarma, A.N.S., Kumar, N., Satyamurty, C., 2001. The deadliest stable continental region earthquake occurred near Bhuj on 26 January 2001. Journal of Seismology 5 (4), 609–615. https://doi.org/10.1023/A:1012228507533.

Sant, D.A., Parvez, I.A., Rangarajan, G., Patel, S.J., Bhatt, M.N., Salam, T.S., 2017. Subsurface profiling along Banni Plains and bounding faults, Kachchh, Western India using microtremors method. J. Asian Earth Sci. 146, 326–336. https://doi.org/10.1016/j.jseaes.2017.06.002.

Sant, D.A., Parvez, I.A., Rangarajan, G., Patel, S., Salam, T.S., Bhatt, M.N., 2018. Subsurface imaging of brown coal bearing Tertiary sedimentaries-Deccan Trap interface using microtremor method. J. Appl. Geophys. 159, 362–373. https://doi.org/10.1016/j.jappgeo.2018.09.008.

Sarkar, D., Sain, K., Reddy, P.R., Catchings, R.D., Mooney, W.D., 2007. Seismic-reflection images of the crust beneath the 2001 M= 7.7 Kutch (Bhuj) epicentral region, western India. Continent. Intraplate Earthq.: Sci. Hazard Pol. Issues 425, 319. https://doi.org/10.1130/2007.2425(20).

Sastry, R.S., Nandini, N., Sarma, S.V., 2008. Electrical imaging of deep crustal features of Kutch, India. Geophys. J. Int. 172, 934–944. https://doi.org/10.1111/j.1365-246X.2007.03658.x.

Savvaidis, A., Smirnov, M.Y., Tranos, M.D., Pedersen, L.B., Chouliaras, G., 2012. The seismically active Atalanti fault in Central Greece: a steeply dipping fault zone imaged from magnetotelluric data. Tectonophysics 554, 105–113. https://doi.org/10.1016/j.tecto.2012.06.002.

Sen, S., Kundan, A., Kalpande, V., Kumar, M., 2019. The present-day state of tectonic stress in the offshore Kutch-Saurashtra Basin, India. Mar. Petrol. Geol. 102, 751–758. https://doi.org/10.1016/j.marpetgeo.2019.01.018.

Seshu, D., Rao, P.R., Naganjaneyulu, K., 2016. Three-dimensional gravity modelling of Kutch region, India. J. Asian Earth Sci. 115, 16–28. https://doi.org/10.1016/j.jseaes.2015.09.015.

Shaikh, M.A., Maurya, D.M., Mukherjee, S., Vanik, N.P., Padmalal, A., Chamyal, L.S., 2020. Tectonic evolution of the intra-uplift Vigodi-Gugriana-Khirasra-Netra Fault System in the seismically active Kachchh rift basin, India: implications for the western continental margin of the Indian plate. J. Struct. Geol. 140, 104124. https://doi.org/10.1016/j.jsg.2020.104124.

Shaikh, M.A., Maurya, D.M., Vanik, N.P., Padmalal, A., Chamyal, L.S., 2019. Uplift induced structurally controlled landscape development: example from fault bounded Jumara and Jara domes in Northern Hill Range, Kachchh, Western India. Geosci. J. 23, 575–593. https://doi.org/10.1007/s12303-018-0061-9.

Shan, X., Yu, Y., Clift, P.D., Tan, C., Jin, L., Li, M., Li, W., 2015. The ground penetrating radar facies and architecture of a paleo-spit from Huangqihai Lake, North China: implications for genesis and evolution. Sediment. Geol. 323, 1–14. https://doi.org/10.1016/j.sedgeo.2015.04.010.

Sheley, D., Crosby, T., Zhou, M., Giacoma, J., Yu, J., He, R., Schuster, G.T., 2003. 2-D seismic trenching of colluvial wedges and faults. Tectonophysics 368, 51–69. https://doi.org/10.1016/S0040-1951(03)00150-1.

Shukla, S.B., Patidar, A.K., Bhatt, N., 2008. Application of GPR in the study of shallow subsurface sedimentary architecture of Modwa spit, Gulf of Kachchh. J. Earth Syst. Sci. 117, 33–40. https://doi.org/10.1007/s12040-008-0010-5.

Shukla, S.B., Chowksey, V.M., Prizomwala, S.P., Ukey, V.M., Bhatt, N.P., Maurya, D.M., 2013. Internal sedimentary architecture and coastal dynamics as revealed by ground penetrating radar, Kachchh coast, western India. Acta Geophys. 61, 1196–1210. https://doi.org/10.2478/s11600-013-0102-8.

Simón, J.L., Arlegui, L.E., Ezquerro, L., Lafuente, P., Liesa, C.L., Luzón, A., 2017. Assessing interaction of active extensional faults from structural and paleoseismological analysis: the Teruel and Concud faults (eastern Spain). J. Struct. Geol. 103, 100–119. https://doi.org/10.1016/j.jsg.2017.08.003.

Stewart, S.A., Argent, J.D., 2000. Relationship between polarity of extensional fault arrays and presence of detachments. J. Struct. Geol. 22, 693–711. https://doi.org/10.1016/S0191-8141(00)00004-3.

Tiwari, P., Maurya, D.M., Shaikh, M., Patidar, A.K., Vanik, N., Padmalal, A., Vasaikar, S., Chamyal, L.S., 2021. Surface trace of the active Katrol Hill Fault and estimation of paleo-earthquake magnitude for seismic hazard, Western India. Eng. Geol. 295, 106416. https://doi.org/10.1016/j.enggeo.2021.106416.

Tokarski, A.K., Świerczewska, A., Lasocki, S., Cuong, N.Q., Strzelecki, P.J., Olszak, J., Kukulak, J., Alexanderson, H., Zasadni, J., Krąpiec, M., Mikołajczak, M., 2020. Active faulting and seismic hazard in the outer western Carpathians (Polish Galicia): evidence from fractured quaternary gravels. J. Struct. Geol. 141, 104210. https://doi.org/10.1016/j.jsg.2020.104210.

Vanik, N., Shaikh, M.A., Mukherjee, S., Maurya, D.M., Chamyal, L.S., 2018. Post-Deccan Trap stress reorientation under transpression: evidence from fault slip analyses from SW Saurashtra, Western India. J. Geodyn. 121, 9–19. https://doi.org/10.1016/j.jog.2018.06.004.

Vanik, N., Maurya, D.M., Shaikh, M., Padmalal, A., Tiwari, P., Chamyal, L.S., 2020. A tectono-geomorphological perspective of micro-earthquake swarm activity prone areas around Bhavnagar and Jamnagar in Saurashtra, western India. Quat. Int. https://doi.org/10.1016/j.quaint.2020.12.041.

Vanneste, K., Radulov, A., De Martini, P., Nikolov, G., Petermans, T., Verbeeck, K., Camelbeeck, T., Pantosti, D., Dimitrov, D., Shanov, S., 2006. Paleoseismologic investigation of the fault rupture of the 14 April 1928 Chirpan earthquake (M 6.8), southern Bulgaria. J. Geophys. Res. Solid Earth 111, B01303. https://doi.org/10.1029/2005JB003814.

Villani, F., Sapia, V., 2017. The shallow structure of a surface-rupturing fault in unconsolidated deposits from multi-scale electrical resistivity data: the 30 October 2016 Mw 6.5 central Italy earthquake case study. Tectonophysics 717, 628–644. https://doi.org/10.1016/j.tecto.2017.08.001.

Wang, Z., Madin, I.P., Woolery, E.W., 2003. Shallow SH-wave seismic investigation of the Mt. Angel fault, Northwest Oregon, USA. Tectonophysics 368, 105–117. https://doi.org/10.1016/S0040-1951(03)00153-7.

Williams, R.A., Stephenson, W.J., Odum, J.K., 2003. Comparison of P-and S-wave velocity profiles obtained from surface seismic refraction/reflection and downhole data. Tectonophysics 368, 71–88. https://doi.org/10.1016/S0040-1951(03)00151-3.

Yeager, K.M., Wolfe, P.C., Feagin, R.A., Brunner, C.A., Schindler, K.J., 2019. Active near-surface growth faulting and late Holocene history of motion: Matagorda peninsula, Texas. Geomorphology 327, 159–169. https://doi.org/10.1016/j.geomorph.2018.10.019.

Zygouri, V., Koukouvelas, I.K., Kokkalas, S., Xypolias, P., Papadopoulos, G.A., 2015. The Nisi Fault as a key structure for understanding the active deformation of the NW Peloponnese, Greece. Geomorphology 237, 142–156. https://doi.org/10.1016/j.geomorph.2013.09.001.